A&A 427, 465–483 (2004)
DOI: 10.1051/0004-6361:20040460

Astronomy & Astrophysics

The B3–VLA CSS sample

IV. kpc-scale polarization properties⋆

C. Fanti[1,2], M. Branchesi[3,2], W. D. Cotton[4], D. Dallacasa[3,2], R. Fanti[1,2], L. Gregorini[1,2], M. Murgia[2,6], C. Stanghellini[5], and M. Vigotti[2]

[1] Dipartimento di Fisica, Universitá di Bologna, via Irnerio 46, 40126 Bologna, Italy
[2] Istituto di Radioastronomia del CNR, via Gobetti 101, 40129 Bologna, Italy
e-mail: m.branchesi@ira.cnr.it
[3] Dipartimento di Astronomia, Universitá di Bologna, via Ranzani 1, 40127 Bologna, Italy
[4] National Radio Astronomy Observatory, Charlottesville, USA
[5] Istituto di Radioastronomia del CNR, CP 141, 96017 Noto SR, Italy
[6] INAF - Osservatorio Astronomico di Cagliari, Loc. Poggio dei Pini, Strada 54, 09012 Capoterra, Italy

Received 17 March 2004 / Accepted 23 July 2004

Abstract. We discuss VLA polarization measurements at 8.5, 4.9 and 1.4 GHz for the B3-VLA sample of Compact Steep-spectrum Sources (CSS). The measurements at the two higher frequencies were presented in a previous paper (Fanti et al. 2001), while those at 1.4 GHz are from the NVSS. The study of the fractional polarization as a function of wavelength shows a variety of behaviours not always accounted for by the current simple models. In a large fraction of sources the integrated rotation angle appears to follow the λ^2 law down to 1.4 GHz, although this conclusion has to be treated with some care due to the small number of polarization measurements. For sources resolved at the two higher frequencies we find that a number exhibit asymmetries in the 8.5 GHz fractional polarization, in depolarization and rotation angle. We discuss depolarization effects and rotation of the polarization angle. We find that Faraday depth effects are very strong within 2−3 kpc of the nucleus, as found earlier by Cotton et al. (2003). A simple model for an external Faraday screen is able to account for the gross observed features. We also find that the Rotation Measure and the Faraday Dispersion appear to increase with the source red-shift.

Key words. galaxies: active – polarization – radio continuum: galaxies – quasars: general – ISM: structure

1. Introduction

Young radio sources, believed to be a significant fraction of the class of **C**ompact **S**teep-spectrum **S**ources (CSS) and **G**igahertz **P**eaked-spectrum **S**ources (GPS) (see O'Dea 1998), owing to their small sizes are fully immersed in the host galaxy inhomogeneous Interstellar Medium (ISM). Clouds with density $n_e \approx 10^4$ cm^{-3}, temperature $T \approx 10^4$ K and small filling factor ($f_0 \approx 10^{-4}$), producing the *Narrow Emission Lines* (*NL*), are distributed up to a kpc from the nucleus. The inter-cloud space is presumed to be filled by a more diffuse and hotter gas component ($n_e \leq 10$ cm^{-3} and $T \geq 10^7$ K) in pressure equilibrium with the *NL* clouds. Strong asymmetries in flux density and arm ratio between the two radio lobes (which cannot be attributed in general to Doppler boosting) are often observed and are explained as interactions of the radio jets with dense gas clumps (see, e.g., Saikia et al. 2001, 2002). Even for moderate magnetic field intensities, significant Faraday Rotation effects are expected from both the diffuse and the clumpy gas. Ordered large scale components of the magnetic field may produce significant Faraday Rotation of the polarization vector as a function of λ^2. On the other hand, inhomogeneities in the density distribution (*NL* clouds) or disordered components of the magnetic field on scales smaller than the source size can produce significant, wavelength dependent, depolarization of the radiation.

CSSs/GPSs have been shown to have large Rotation Measures and large depolarizations (see, e.g., O'Dea 1998, and references therein). Such sources are thus powerful tools in the study of the kpc properties of their host galaxy ambient medium.

In this paper, we present the polarization characteristics of a complete sample of CSSs, the *B3–VLA CSS sample*, at the three frequencies of 8.5, 4.9 and 1.4 GHz, and discuss the implications on the properties of the external medium.

Section 2 gives a short summary of the B3–VLA CSS sample.

Sections 3 and 4 describe the polarization data reduction and the results respectively.

⋆ Tables A1, A2 and A3 are only available in electronic form at http://www.edpsciences.org

Sections 5 and 6 present a discussion of the major results obtained and the conclusions.

Appendix A contains the more extended data tables.

2. The B3–VLA CSS sample

The present CSS sample, described in Fanti et al. (2001, Paper I), was selected from the *B3–VLA catalogue* (Vigotti et al. 1989). It consists of 87 CSSs/GPSs with linear sizes (LS) in the range[1] $0.4\ h^{-1} \leq$ LS (kpc) $\leq 20\ h^{-1}$ and with radio luminosity $P_{0.4\ \mathrm{GHz}} \geq 10^{26}\ h^{-2}$ W/Hz.

The sample has been observed with the VLA at 1.4 GHz, in A and C configurations, without polarization information (Vigotti et al. 1989) and at 4.9 and 8.5 GHz in full polarization (both A configuration; Paper I). In addition NVSS data at 1.4 GHz (Condon et al. 1998), complete with polarization information, are available for the majority of the sources. Three sources (1014+392, 1141+466, 1445+410) do not have polarization measurements at high frequencies, hence the sample discussed here consists of 84 objects only.

A number of sources, unresolved or poorly resolved even at the highest VLA resolution (≈0.2″ at 8.5 GHz) were observed in two separate VLBI projects at 1.7 GHz (Dallacasa et al. 2002a,b; Papers II and III) and in a third at 5 and 8.5 GHz (Orienti et al. 2004, Paper V).

The total source sample is presented in Table A.1, with data taken from the above papers. Red-shifts are either spectroscopic or photometric from *K* or *R* band. When no red-shift is available, $z = 1.05$ has been assumed through the whole paper, as discussed in Paper I. A simple morphological classification is also given. The terms *CSO* (Compact Symmetric Object) and *MSO* (Medium Symmetric Object) refer to a double sided morphology and a projected linear size smaller or larger than $\approx 1\ h^{-1}$ kpc, as introduced by Fanti et al. (1995) and Readhead et al. (1996). Thirteen of the sources that have an uncertain morphological type and are not classified as *MSO* or *CSO* are still listed in Table A.1 but are marked with a †. Source comments are included as necessary.

3. Polarization data reduction

The polarization data, presented in Paper I, have been reanalized as follows:

i) The 8.5 GHz images were smoothed to the resolution of those at 4.9 GHz (∼0.4 arcsec) by convolving and regridding the images in the Stokes parameters *I*, *U*, and *Q*. From the convolved *Q* and *U* images we produced new $P = \sqrt{U^2 + Q^2}$ images. Careful checks were made in order to have the images at the two frequencies well registered. Shifts in position, due to phase self-cal, are usually ≤0.05 arcsec but can reach ∼0.10″. In these cases, the images were registered using bright optically-thin features as a positional reference. After these corrections the images are aligned to within ∼10% of the beam size. The new images are not shown here since they do not contribute significantly to the information presented in Paper I.

ii) Polarization parameters of source sub-components were computed in the same areas on the two frequency images (Sect. 3.1).

iii) A more careful evaluation has been made of the instrumental polarization, which in Paper I was, conservatively, estimated to be 0.3% rms. The residual instrumental polarization was estimated following Condon et al. (1998) from the peak of the distribution of the fractional polarization of the strongest sources ($S_{4.9}$ and $S_{8.5} \geq 200$ mJy). This technique assumes that the strongest sources are unpolarized; since this is less true at high than low frequencies, our estimate of the instrumental polarization will be larger than the true value. We found residual rms instrumental polarizations of 0.15% and 0.20% at 4.9 and 8.5 GHz respectively.

iv) A statistical correction, dependent on the signal to noise ratio, has been applied to the polarized flux densities in order to correct for the *polarization bias* (Wardle & Kronberg 1974; Simmons & Steward 1985; Condon et al. 1998)

In this paper we use two different approaches to the data analysis, aimed at highlighting different characteristics of the polarized radiation.

In the first approach, referred to as *low resolution*, we use an angular resolution such that all sources appear unresolved. This allows us to compare these *low resolution* data with the data at 1.4 GHz from the NVSS (Condon et al. 1998).

In the second approach, referred to as *high resolution*, we have considered the fifty most resolved sources and have split them into independent components. In thirty-five sources the splitting was into two major components, interpreted as the radio lobes. In the fifteen more extended radio sources additional sub-structure is present, either in the lobes or as an additional central component, and a further sub-division has been made.

Given the wide range of angular sizes (<0.2″−6″) this broad component sub-division is aimed at providing approximately the same number of resolution elements for each subcomponent. We stress that, due to the limited resolution, these components are not necessarily homogeneous. It is therefore likely that there is a mixing of lobes with hot spots and fragments of jets. Inner components of multiple sources may be jets or sub-structures of lobes and so on.

For image handling we used the NRAO Astronomical Image Processing System (AIPS).

3.1. Polarization parameters

For each source (or component) we have computed at both 8.5 and 4.9 GHz the flux density for total intensity S_I and linear polarization S_P, and the average position angle χ of the $\boldsymbol{E}$ vector. Linear polarization was computed with both *scalar* and *vectorial* averaging, i.e. averaging in polarization, *P*, or in *Q* and *U* (see below). Subsequently, fractional polarization, $m = S_\mathrm{P}/S_\mathrm{I}$, rotation angle, $\Delta\chi^{\nu 2}_{\nu 1} = \chi_{\nu 2} - \chi_{\nu 1}$, and depolarization ratio, $DP^{\nu 2}_{\nu 1} = m_{\nu 2}/m_{\nu 1}$, between pairs of frequencies ($\nu_2 < \nu_1$) have been derived.

For the *high resolution data* flux densities from *I*, *P*, *Q* and *U* images were computed using the following procedure. Around each major component visible on the *I* image

[1] $H_0 = 100\ h$ km s^{-1} Mpc^{-1}, $q_0 = 0.5$.

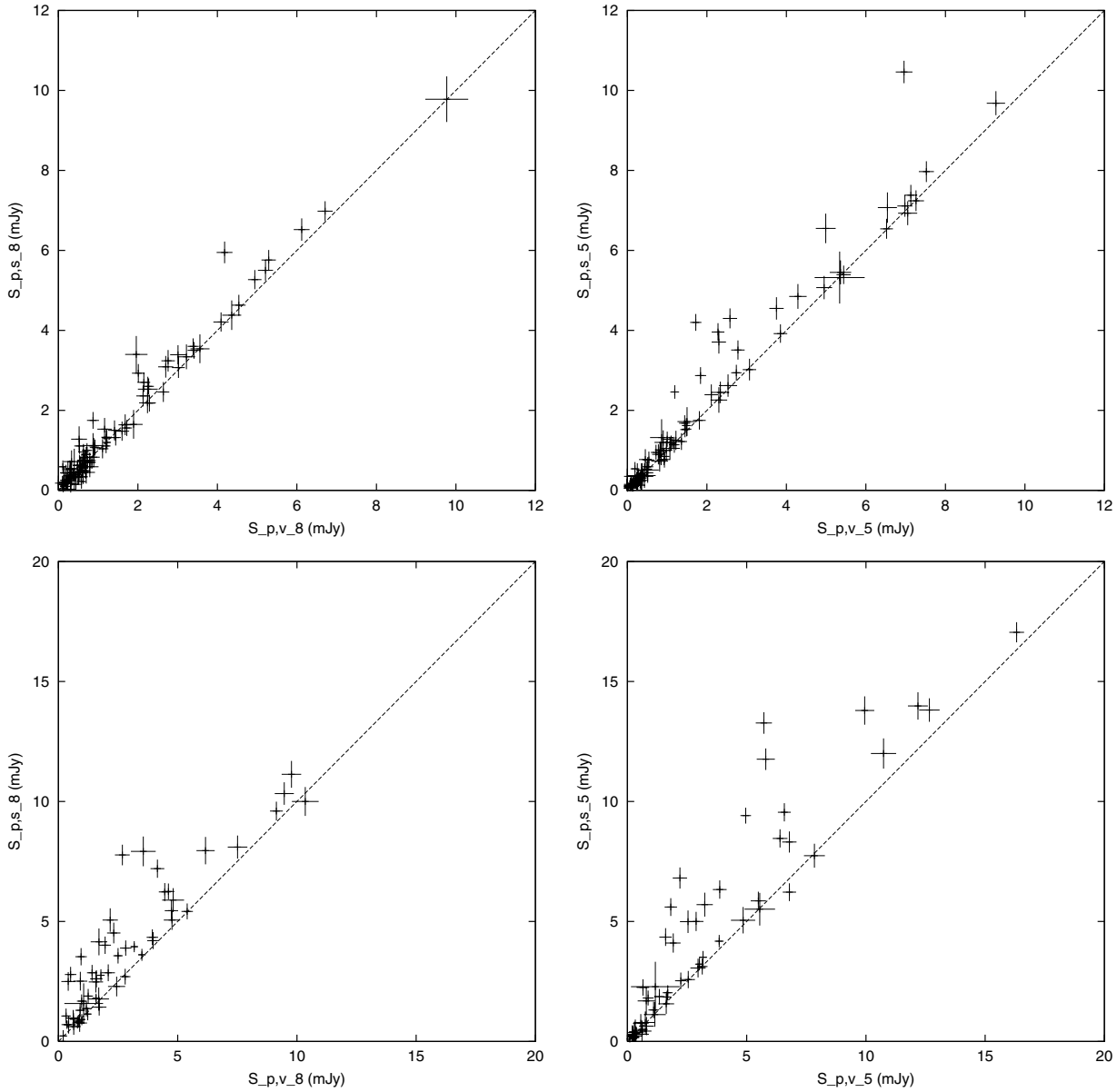

Fig. 1. $S_{\rm P}^{\rm s}$ vs. $S_{\rm P}^{\rm v}$ for components of resolved sources *(top)* and for the whole source (*bottom*), at 8.5 GHz (*left*) and 4.9 GHz (*right*). Note that, for clarity, the source 2311+269 has not been included since it has a polarized flux $\gtrsim$25 mJy. The dotted line is for $S_{\rm P}^{\rm v} = S_{\rm P}^{\rm s}$. The crosses represent the 1-σ error bars.

a rectangular area or "box" was set, which was the same at the two frequencies and for all the images of each source. The integrated flux densities were then derived via the AIPS task IMEAN as:

$$S_{\rm I} = \sum_{ij} I_{ij}/\Omega_{\rm b}\,; \qquad S_{\rm P}^{\rm s} = \sum_{ij} P_{ij}/\Omega_{\rm b} \quad (\textit{scalar})$$

$$S_{\rm Q} = \sum_{ij} Q_{ij}/\Omega_{\rm b}\,; \quad S_{\rm U} = \sum_{ij} U_{ij}/\Omega_{\rm b}$$

where ij is the image pixel coordinate and $\Omega_{\rm b}$ is the beam area. We also computed the *vector* polarized flux density and the associated mean position angle of the electric vector as:

$$S_{\rm P}^{\rm v} = \sqrt{S_{\rm U}^2 + S_{\rm Q}^2}\,; \quad \chi = \frac{1}{2}\tan^{-1}\left(\frac{S_{\rm U}}{S_{\rm Q}}\right).$$

The computation of the *vector* flux density, $S_{\rm P}^{\rm v}$, in place of the *scalar* flux density, $S_{\rm P}^{\rm s}$, has the disadvantage of causing depolarization if there are rotations of the electric vector within the "box" itself. In the *high resolution* analysis the components into which we have split a source are usually not much larger than the beam, hence the differences are minor, $S_{\rm P}^{\rm s}$ being higher than $S_{\rm P}^{\rm v}$ by $\sim(5 \pm 3)$% and $\sim(5 \pm 5)$% at 8.5 and 4.9 GHz respectively (Fig. 1, top panels). The more discrepant few points at 8.5 GHz and the larger dispersion at 4.9 GHz are likely due to differential rotation of the electric vector in the slightly extended source components. Given the close similarity of $S_{\rm P}^{\rm s}$ and $S_{\rm P}^{\rm v}$ for the majority of the source components in the *high* resolution analysis, we give in Table A.2 only the *vector* fractional polarization, $m_{\rm v} = S_{\rm P}^{\rm v}/S_{\rm I}$.

For the *low resolution* analysis the polarization parameters I, Q, U and $S_{\rm P}^{\rm v}$ were computed by integration (AIPS task "IMEAN") on a box which includes all the visible emission on the I images. In Fig. 1 (bottom panels) we compare the integrated scalar and vector polarized flux densities at the two frequencies. There are clearly several sources with $S_{\rm P}^{\rm s} \geq S_{\rm P}^{\rm v}$ due to changes in the polarization position angle from one component to another. Since we are comparing our results with integrated polarization measurements from the NVSS (Condon et al. 1998), $S_{\rm P}^{\rm v}$ is the appropriate value to use because the NVSS catalog essentially uses the same measure.

3.2. Errors

The radio brightness distribution in "empty" regions of I, Q and U images is approximately Gaussian, therefore we can assume the rms as a good noise estimate. Typical values (1σ) are $\sigma_{\rm Q,U} \approx 0.08$ mJy/beam for Stokes parameters Q and U and $\sigma_{\rm I} \approx 0.1$ mJy/beam for I. For extended components we take as flux errors $\sqrt{N}$ times the above quoted values, where N is the number of independent beam areas across the structure. The errors of the derived parameters are computed from these values using the error propagation. We have:

$$\sigma_{m^{\rm v}} \approx \frac{\sigma_{\rm QU}}{S_{\rm I}};\ \sigma_{\chi} \approx \frac{1}{2}\frac{\sigma_{\rm QU}}{S_{\rm P}^{\rm v}};$$

$$\left[\frac{\sigma_{DP}}{DP}\right]^2 \approx \left(\frac{\sigma_{\rm QU}}{S_{\rm P}^{\rm v}}\right)^2_{\nu_2} + \left(\frac{\sigma_{\rm QU}}{S_{\rm P}^{\rm v}}\right)^2_{\nu_1};$$

$$\left(\sigma_{\Delta\chi}\right)^2 = \left(\frac{\sigma_{\rm QU}}{2S_{\rm P}^{\rm v}}\right)^2_{\nu_2} + \left(\frac{\sigma_{\rm QU}}{2S_{\rm P}^{\rm v}}\right)^2_{\nu_1}.$$

We point out that in the above derivations we have neglected terms involving $(\sigma_{\rm I}/I)^2$ since the *S/N* on I images at both frequencies is always much greater than the corresponding *S/N* on polarized images.

The rms of the instrumental polarization has been added quadratically to the polarization noise to obtain the final errors. Finally, very conservatively, a calibration error of 2° has been quadratically added to the noise error of the polarization position angle

In order to check the reliability of our error estimates we have compared our low resolution measures at 8.5 and 4.9 GHz with those of Klein et al. (2003) at 10.5 and 4.8 GHz, from the Effelsberg radio telescope, for sixteen common sources for which these data are available. The rms of the differences in polarized flux density and in angle are consistent with the estimated errors (Table 1).

4. Results

The polarization parameters of resolved source components (*high resolution*) and the integrated polarization parameters (*low resolution*) including the data at 1.4 GHz from the NVSS are given in the Appendix (Tables A.2 and A.3 respectively). In both these Tables, at each frequency we give: component or total source flux density ($S_{\rm I}$), vector fractional polarization ($m_{\rm v}$) and position angle (χ), defined within ±90°, with the corresponding errors in brackets[2]. The $\boldsymbol{E}$ vector position angle has an intrinsic ambiguity of ±180° due to its definition. This is taken into account in the evaluation of the Rotation Measure (*RM*) in Sect. 4.3.

Table 1. Comparison of present polarization data with Klein et al. (2003).

Difference	rms	
	Found	Expected
$\chi_{8.5} - \chi_{10.5}$	11°	13°
$\chi_{4.8} - \chi_{4.9}$	9°	7°
$S_{p_{8.5}} - S_{p_{10.5}}$	1.6 mJy	1.4 mJy
$S_{p_{4.8}} - S_{p_{4.9}}$	1.9 mJy	1.8 mJy

Table 2. Percentage of polarized sources at *low resolution*.

8.5 GHz	4.9 GHz	1.4 GHz	$m_{\rm v}/\sigma_{m_{\rm v}}$
73%	65%	58%	≥2
64%	58%	47%	≥3
51%	42%	32%	≥5

We note that bandwidth depolarization has a minor effect at 8.5 and 4.9 GHz, unless very high Rotation Measures (≥10^4 rad/m^2) are present, while in the NVSS bandwidth depolarization is expected to be quite large already for $RM \geq 200$ rad/m^2 (Condon et al. 1998).

4.1. Fractional polarization

As seen in Tables A.2 and A.3 a large fraction of the sources have a significant polarization at the three frequencies. Table 2 shows the situation for $m_{\rm v}$ at *low resolution* for increasing value of *S/N* ratio.

In the *high resolution* images the rates of polarized component detection at the two higher frequencies are somewhat higher, by up to 10%, for all *S/N* ratios.

We often find large asymmetries at 8.5 GHz in the fractional polarization of the outer components, ≥20% of sources having ratios in $m_{\rm v}^8 \geq 5$. There is a tendency for the components weaker in total intensity to have a larger $m_{\rm v}^8$. We find no significant differences amongst quasars, galaxies and empty fields.

4.2. Depolarization

Comparison of the fractional polarization at the various frequencies, both for the *low resolution* and for the *high resolution* data, shows that a number of sources display a fractional polarization which increases with frequency. The effect, measured by the depolarization ratio $DP_{\nu 1}^{\nu 2} = m_{\nu 2}/m_{\nu 1}$, is clearly detected between 4.9 and 8.5 GHz and is even more significant between 1.4 and 8.5 GHz.

[2] Only the noise error is given for $S_{\rm I}$.

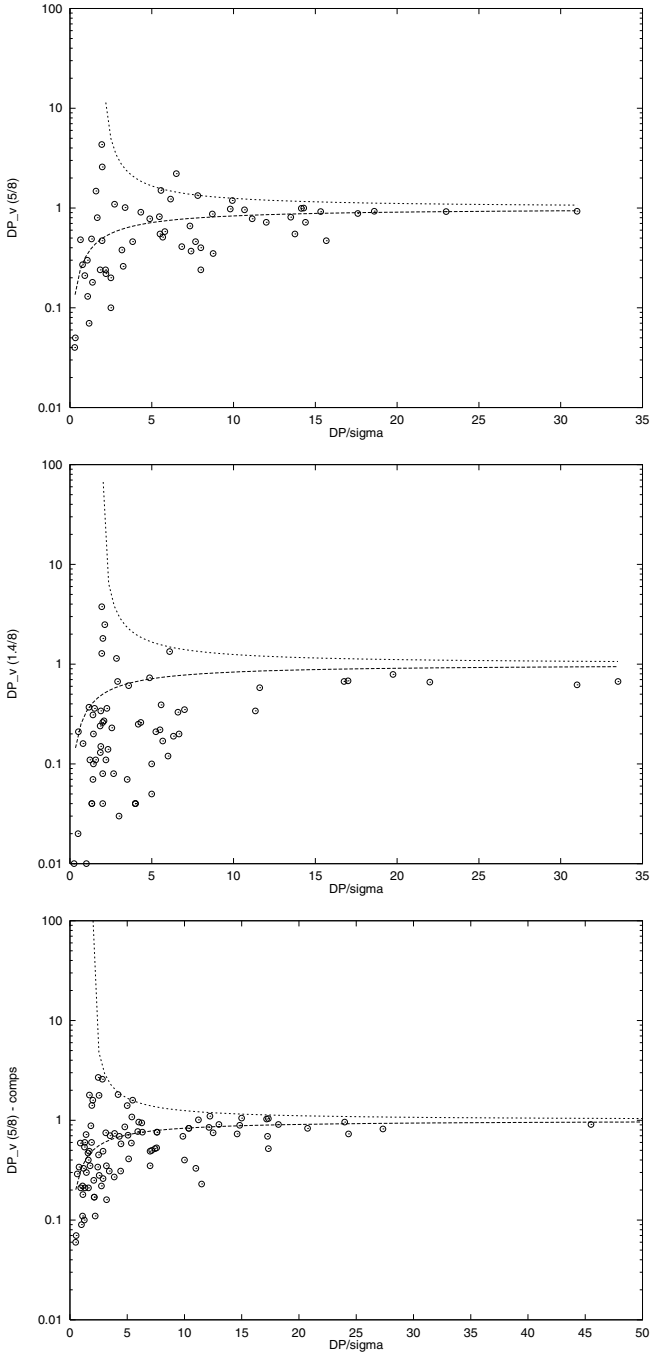

Fig. 2. Depolarization versus *S/N*: at low resolution on *top* (4.9/8.5 GHz) and *central* (1.4/8.5 GHz) panels; at high resolution (4.9/8.5 GHz) on *bottom* panel. In all figures the two lines show the upper and lower bounds of the 95% (2σ) confidence interval of statistical fluctuations in the absence of depolarization ($DP = 1$).

As the significance of $DP^{\nu 2}_{\nu 1}$ depends on the signal to noise ratio for $S_{\rm P}$ at the two frequencies (Sect. 3.2), we show in Fig. 2 plots of the *low resolution* depolarization ratio as a function of $DP/\sigma_{\rm DP}$. The regions above and below the dashed lines contain those objects whose DP differs from 1 (=no depolarization) by more than 2σ. It is clear that the fraction of sources which show a decrease in the fractional polarization with wavelength is rather large: ≈50% for the frequency pair 4.9/8.5 GHz and ≈75% for the pair 1.4/8.5 GHz. Note that, except for one case (1025+390B, see Fig. 2, top panel), values of $DP > 1$ are not significant.

The same plot for the components of the well resolved sources (*high resolution* data) is also shown in Fig. 2. It is clear from the figure that large depolarization effects (small DPs) are already present at the level of individual components. Some of the components appear to exhibit re-polarization effects; these however, are not statistically significant.

Finally at *high resolution* we find that in more than 30% of the sources the components show significant differences in depolarization from each other.

4.3. Rotation of the polarization angle and rotation measures

In most sources, at both *low* and *high resolution*, the polarization position angle shows significant changes with the frequency which is indicative of Faraday Rotation effects, either due to our own Galaxy or intrinsic to the source.

We have estimated the Milky Way contribution from the data set of Rotation Measures from Klein et al. (2003) which contains about 200 sources carefully measured at 4 frequencies in the same sky area of our sources. From this data set it is clear that the Galactic rotation $\Delta\chi^{4.9}_{8.5}$ is $\approx -10^\circ \pm 3^\circ$ in the range $23^{\rm h} \leq$ RA $\leq 3^{\rm h}$ and $\approx +1.3^\circ \pm 0.2^\circ$ in the range $7^{\rm h} \leq$ RA $\leq 15^{\rm h}$ corresponding to $RM \approx -70$ rad/m^2 and $RM \approx +9$ rad/m^2 respectively.

In Fig. 3 we show the distribution of the absolute values of the rotation angles $|\Delta\chi|^{4.9}_{8.5}$ (taken within ±90°) corrected for the Galactic rotation for sources (*low resolution*) and for components (*high resolution*) whose estimated errors on $\Delta\chi$ are ≤12°.

In ≈45% of cases the rotation angle for both components and for the entire source, corrected for the average Galactic rotation, is >15°, corresponding to an $RM \geq 110$ rad/m^2.

We have used the polarization angles of Table A.3 (*low resolution* data) to derive a three-point Faraday Rotation Measure, RM_3, by weighted linear interpolation of the data with the law $\chi(\lambda) = \chi_0 + \lambda^2 RM$. The procedure has been applied to those 31 sources whose polarized flux density is $\geq 3\sigma$ at 8.5 and 4.9 GHz and $\geq 2\sigma$ at 1.4 GHz. Note that these sources typically have linear sizes ≥5 kpc (see Sect. 4.5). We have assumed that between 8.5 and 4.9 GHz any rotation is less than 180°. This assumption implies that RMs $\geq$ 1300 rad/m^2 would be missed. Selected examples of these fits, discussed below, are shown in Fig. 4.

The range covered in λ^2 by the three sets of data is not optimal since the two short wavelengths are rather close to each other and well separated from the third long one. In this situation, even when the errors on $\Delta\chi^{4.9}_{8.5}$ are ≤5° there may be ambiguities in $\chi_{1.4}$ of 180° or 360°. In the fit we searched for solutions for RM_3 with chi-square ≤3. In a number of cases we found more than one acceptable solution, corresponding to different $n_{1.4} \times 180^\circ$ ambiguities in $\chi_{1.4}$ (see, e.g., 0137+401 in Fig. 4). The RM_3s (not corrected for the Galactic Faraday rotation, $RM_{\rm obs}$), derived with the smallest $|n_{1.4}|$ are given in Table 3 together with other acceptable values of $n_{1.4}$. Note that an

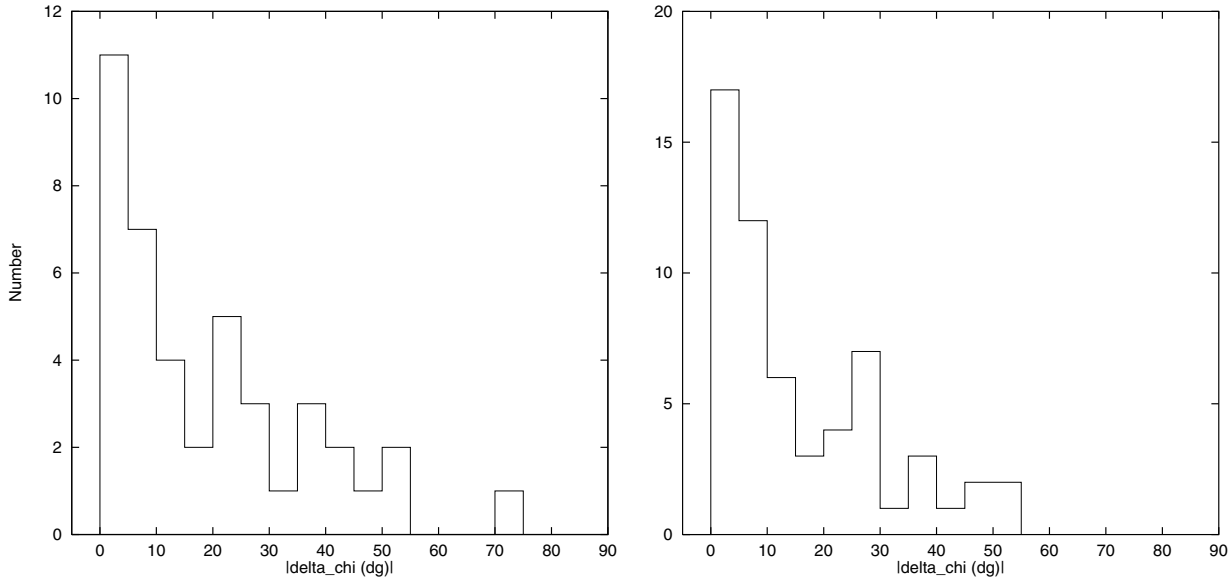

Fig. 3. Distribution of the $|\Delta\chi|^{4.9}_{8.5}$ at low resolution (*left*) and at high resolution (*right*), corrected for Galactic rotation, for sources and components with errors on $\Delta\chi \leq 12°$.

uncertainty $\delta|n_{1.4}| = 1$ implies an uncertainty $\delta|RM| \approx 72$ rad/m^2. In 36% of cases no ambiguity in $\chi_{1.4}$ was present (i.e. $n_{1.4} = 0$) and in 45% we needed to add or subtract one turn of phase in polarization angle at 1.4 GHz

The formal errors on RM_3 are very small, of the order of a few rad/m^2. The actual uncertainties are the $n_{1.4}$ ambiguities and the assumption of validity of the λ^2 law over the whole wavelength range.

The source frame (sf) Rotation Measure, obtained from the Galaxy-corrected Rotation Measure by multiplying it by $(1 + z)^2$, is also given in Table 3.

The RM_3 distribution (Fig. 5), compared with the distribution of $\Delta\chi^{4.9}_{8.5}$ (Fig. 3), shows some deficiency of values above 200 rad/m^2. This is possibly due to the fact that for larger values of RM the fractional polarization at 1.4 GHz drops quickly because of bandwidth depolarization (see Fig. 7) and RM_3 cannot be computed. Therefore sources with RM above that value may be under-represented.

In order to check the reliability of our RM_3s, we have compared them with the RMs of Klein et al. (2003) for the ten sources in common for which these data are available. Note that Klein et al. (2003) also have polarization data at 2.7 GHz, which allows them to drastically reduce the $n_{1.4} \times 180°$ ambiguities.

For five sources (marked by an * in Table 3) the agreement of our measurements with those of Klein et al. (2003) is very good (see, e.g., † 0110+401 or 0805+406 in Fig. 4). A sixth source (1220+408, Fig. 4) is also marked by an * since the difference between the two Rotation Measures, larger than the combined uncertainties, is attributable to the fact that Klein et al. (2003) did not use the NVSS measure, which we used. Our Rotation Measure (see Fig. 4) provides an acceptable fit across the whole set of data. For the source 0213+412 (Fig. 4), marked by **, our Rotation Measure is inconsistent with the polarization angle at 2.7 GHz, while that of Klein et al. (2003) is inconsistent with the polarization angle at 1.4 GHz, that they did not use in their fit. A good model that fits all the data is obtained by allowing for a 180° ambiguity at 2.7 GHz and by taking $n_{1.4} = -2$ (still acceptable, Table 3). This model is represented by the dot-dashed line in Fig. 4.

For two sources, † 0809+404 and † 1343+386, where again Klein et al. (2003) did not use the NVSS measure, the large disagreements are reduced by taking $n_{1.4} = -2$ and -1 respectively (dotted line in Fig. 4), which were not considered in our initial fits since they gave an excessive chi-square with our own data alone. Finally, in the case of 0955+390 it seems that a deviation from the λ^2 law is occurring at $\lambda > 11$ cm (see Fig. 4). These three last sources are marked by "no" in Table 3.

The comparison suggests that more than half of our RM_3 are correct, but it also points out the importance of having measures at a wavelength intermediate between 6 and 20 cm in order to reduce the effects of the $n_{1.4} \times 180°$ ambiguities. Thanks to the availability of data at four wavelengths, it seems fair to conclude that most sources follow the λ^2 law in the range from 2.8 to 20 cm.

If we correct the observed Rotation Measures by the factor $(1 + z)^2$ (assuming $z = 1.05$ for the sources without redshift) we get the *intrinsic Rotation Measures* (source frame, sf), reported in Table 3. About 50% of the sources have intrinsic $RM \leq 200$ rad m^{-2}, but ≈20% have $RM \geq 1000$ rad m^{-2}.

Using the *high resolution* data we compared the rotation angle $\Delta\chi^{4.9}_{8.5}$ of the individual components within the same object. In eight sources (0120+405, 0144+432, 0222+422, 0814+441, 1025+390B, †1039+424, 1201+394, 1220+408) there is a significant difference in the range of ≈20°−50° between the rotation angles of the two components. More generally the distribution of the differences of the $\Delta\chi^{4.9}_{8.5}$ of the two components is significantly broader than expected from the estimated errors and implies a dispersion of ≈15°−20° in the differential

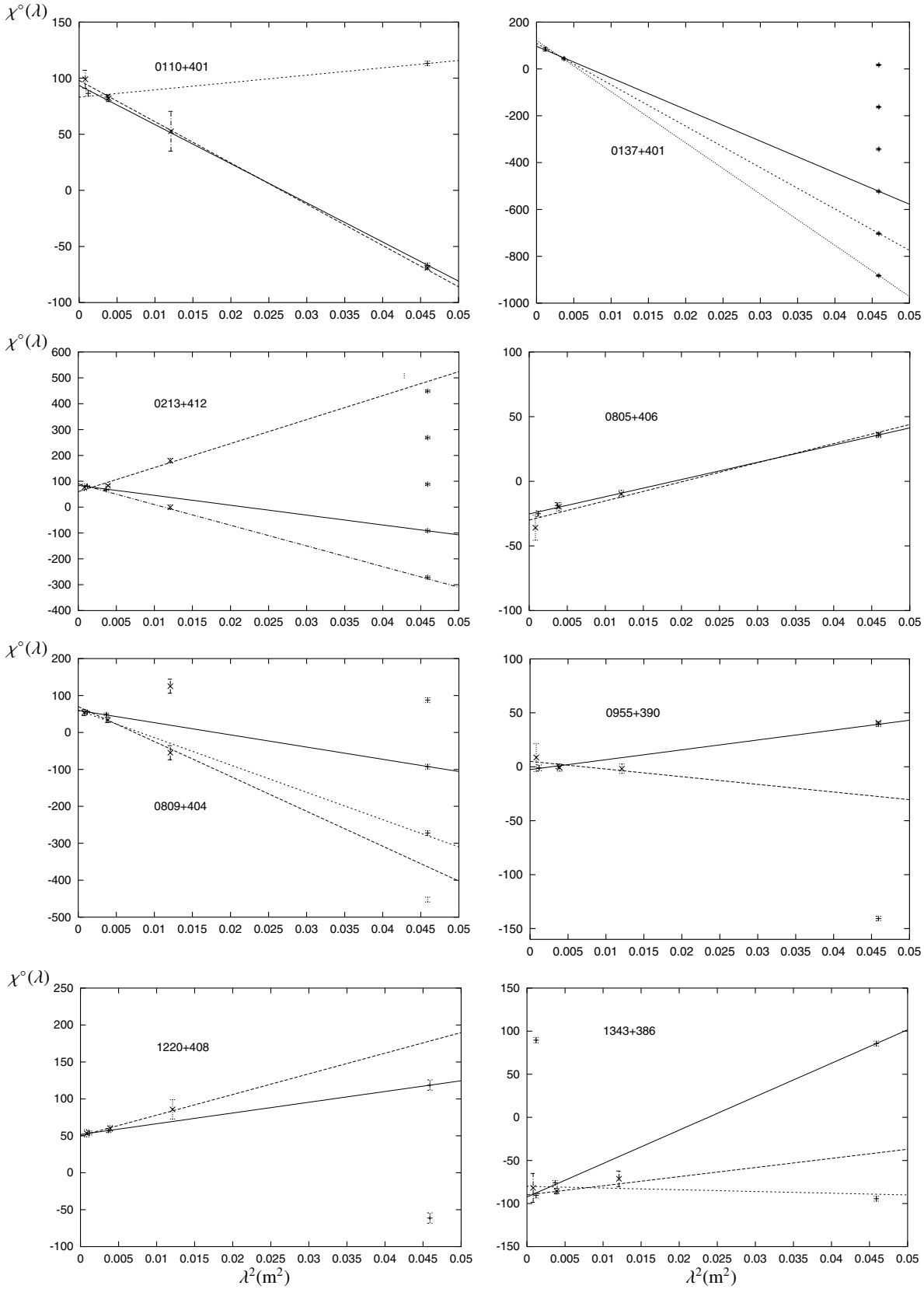

Fig. 4. Examples of $\chi(\lambda)$ vs. λ^2 fits discussed in the text. A + mark our own data, an × those from Klein et al (2003). The continuous and the long dashed lines correspond to the RM_3 given in Table 3 and to the RM of Klein et al. (2003), respectively. Other lines are alternative fits. $n_{1.4} \times 180°$ ambiguities at 1.4 GHz are also marked. Note the role of the datapoint at 2.7 GHz ($\lambda^2 = 0.0123$ m^2).

Table 3. Observer's and source's frame three-frequency Rotation Measures and $n_{1.4} \times 180°$ ambiguities.

	Name	RM_{obs}	RM_{sf}		$n_{1.4}$			Name	RM_{obs}	RM_{sf}		$n_{1.4}$	
†	0034+444	59	1850		1		†	0809+404	−56	−156	no	−1	
	0039+412	−98	[−118]		−1			0930+389	33	3800		4	5
†	0110+401	−61	55	*	0	1		0951+422	78	533		1	2
	0120+405	−378	− 1043		−5			0955+390	16	[29]	no	0	
	0137+401	−235	− 1133		−3	−4, −5	†	1039+424	13	[17]		0	
	0144+432	−56	72		−1	−2	†	1055+404A	9	[0]		0	
	0213+412	−67	7	**	−1	−2		1201+394	33	50		0	1
	0222+422A	75	2940		1	2,3		1216+402	−117	−347		−1	−2
	0228+409A	−14	[235]		0	−1		1220+408	25	[67]	*	1	
	0254+406	−25	221		0	1		1233+418	− 10	−8		0	
	0701+392	254	1230		4	5,6	†	1343+386	68	476	no	0	1
	0744+464	−276	− 4400		−3	−4		1350+432	152	1419		2	3
†	0748+413B	−45	[−227]		−1			1458+433	− 5	−52		0	
†	0754+396	4	− 49	*	1			2304+377	96	956	*	1	
†	0800+472	−18	[−113]	*	−1	−2		2311+469	66	416		1	
	0805+406	23	[65]	*	0								

A † marks sources not classified as *CSO* or *MSO* (see Table A.1). [RM_{sf}] is for sources without red-shift (z = 1.05 assumed). Note that RM_{sf} is corrected for Galactic *RM* whereas RM_{obs} is not. The fourth column contains an * for sources for which we obtain good agreement with Klein et al. (2003), ** indicates compatible results when the NVSS data is included, "no" indicates plausible agreement with a fit of our data that gives an excessive chi-square, see present Sect. 4.3. The sixth column contains alternative, plausible number of turns of phase to add to the 1.4 GHz polarization angles.

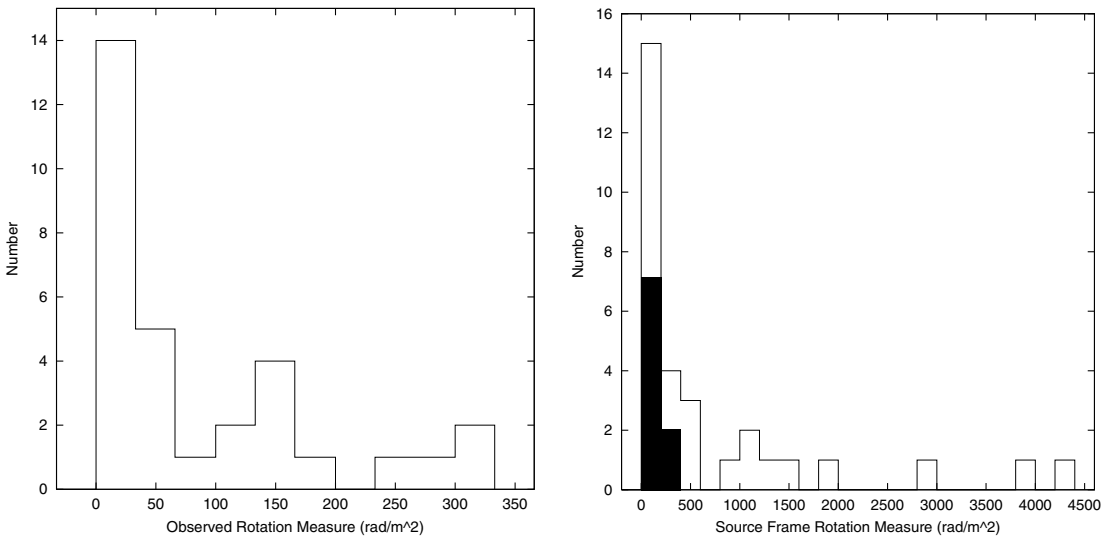

Fig. 5. Distribution of three-frequency $|RM_3|$. *Left* panel is for the observer frame (Galaxy corrected). Note that RM_3 = 100 rad/m^2 corresponds to $\Delta\chi^{4.9}_{8.5} \sim 14°$. *Right* panel is for the source frame. Dark bars indicate sources without red-shift for which z = 1.05 has been assumed.

rotation between components, corresponding to a dispersion in the differential Rotation Measures ≥100 rad m^{-2}.

Inside each source component there are probably smaller regions with different Rotation Measures so that the rotation angle we see is an "average value". In such a situation the average polarization angle is not expected to change as λ^2. It is therefore of note that so many sources (≈50% of those measured at 2.7 GHz) follow the λ^2 law.

4.4. Depolarization and rotation measure

We have searched for a correlation between depolarization and (Galaxy-corrected) rotation angle both in the *high resolution* and on the *low resolution* data.

Figure 6 shows plots of the depolarization ratio $DP^{4.9}_{8.5}$ vs. the rotation angle $\Delta\chi^{4.9}_{8.5}$, with both *low resolution* and *high resolution* data, for the sources/components with $m^8_v > 3\sigma$ and whose estimated errors on $\Delta\chi$ are ≤20°. More depolarized

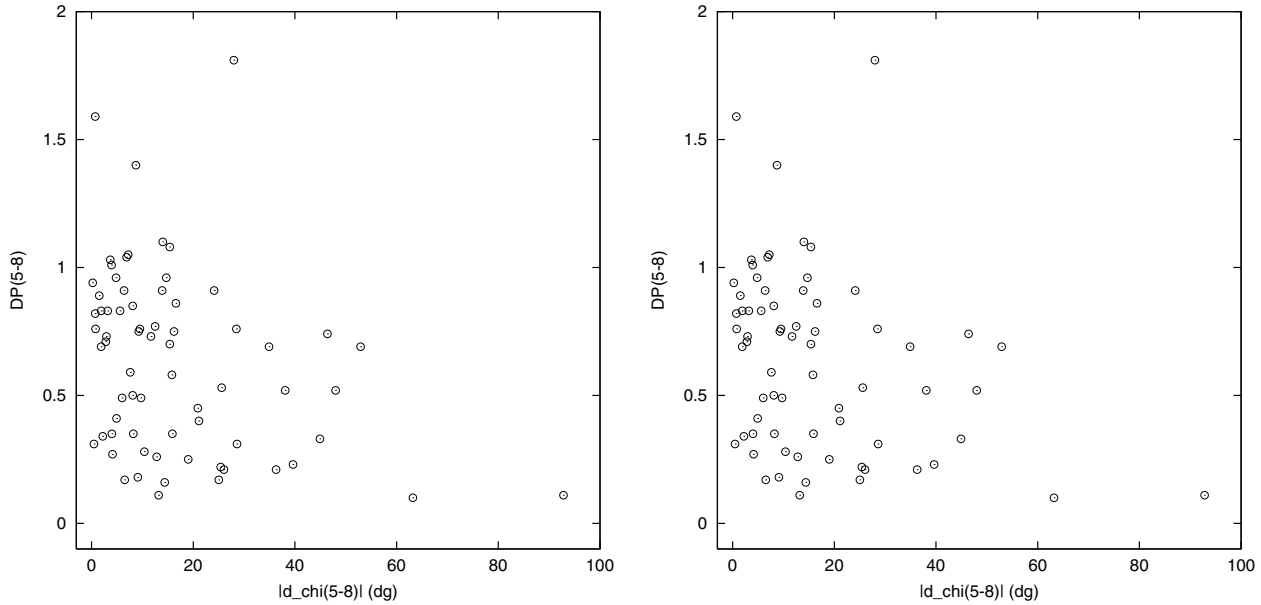

Fig. 6. Depolarization ratio vs. rotation angle (4.9/8.5 GHz) (Galaxy corrected) at high (*left*) and low (*right*) resolutions.

sources ($DP^{4.9}_{8.5} \leq 0.7$) show a broader distribution of rotation angles as compared to the less depolarized ones. Chi-square tests on contingency tables show that the probability that this effect is spurious is ≤1%.

Figure 7 displays the plot of $DP^{1.4}_{8.5}$ vs. $|\Delta\chi^{4.9}_{8.5}|$. The curve on the plot shows the expected effect of bandwidth depolarization at the lowest frequency (Condon et al. 1998) on the assumption of a Rotation Measure in the 1.4 GHz band equal to the one derived from our high frequency data. The large majority of sources are significantly below this curve, showing that bandwidth depolarization is not the major cause of depolarization. There are no sources with a *DP* significantly above the curve except in the region around its deep minimum. This suggests either that the expected bandwidth depolarization is overestimated in that range of Rotation Measures, or that the high frequency *RM* does not apply at the lowest frequency.

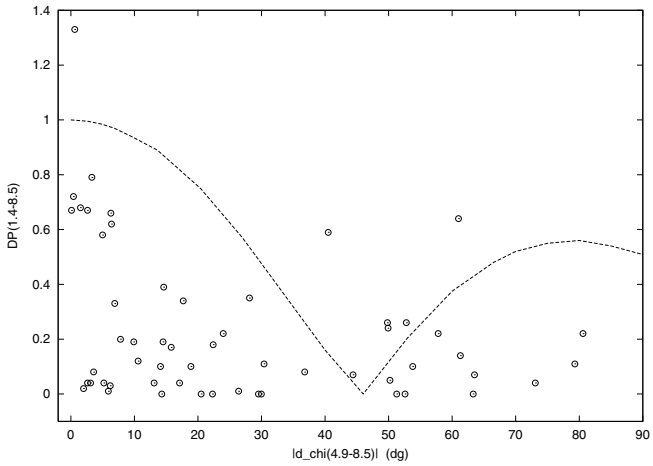

Fig. 7. Depolarization (1.4/8.5 GHz) vs. rotation angle (4.9/8.5 GHz). The line represents the effect of bandwidth depolarization at 1.4 GHz (Fig. 23 in Condon et al. 1998).

4.5. Linear size dependence of fractional polarization

Cotton et al. (2003) have examined the NVSS (1.4 GHz) polarization data of this sample as a function of the source projected linear size, LS, and found that the fractional polarization of the sources with LS ≤ 6 kpc is very small, always less than 1% and typically ≤0.4%. Above ≈6 kpc this changes abruptly and settles on a median value of about 0.9%, with a large dispersion and values up to 4−5%.

In Fig. 8 we plot m_v at 1.4 GHz, 4.9 and 8.5, taken from Table A.3, as a function of LS. The horizontal segments show the median values for intervals of LS. At all LSs, the distribution of the m_v has a rather large dispersion and is quite skewed at all frequencies. The discontinuity of the fractional polarization at around 5 kpc is very evident in all three panels, although at 4.9 and 8.5 GHz a few of the smallest objects do show significant polarization. The curves represent models discussed in Sect. 5.4.

The mean and median values of m_v at the three frequencies for classes of LS are reported in Table 4. We note that ten of the thirteen sources not classified as *CSO*s or *MSO*s have fractional polarization definitely in excess of the mean or median values of their size class. In computing the mean and median values we have included these ten sources.

In Fig. 9 we plot the depolarization ratios $DP^{4.9}_{8.5}$ and $DP^{1.4}_{8.5}$ as a function of LS. The curves represent models discussed in Sect. 5.4. Trends similar to those in Fig. 8 are observed. It is also seen that a few *small sources* with significant polarization at 8.4 and 4.9 GHz do have strong depolarization.

In Table 5 we give mean and median values of *DP* for classes of LS. For comparison purposes we have added the corresponding values for forty-five sources with LS > 40 kpc from the sample of Klein et al. (2003). We have not considered the size range LS ≤ 1 kpc since about half of the sources are not polarized at all three frequencies. As it is likely that this

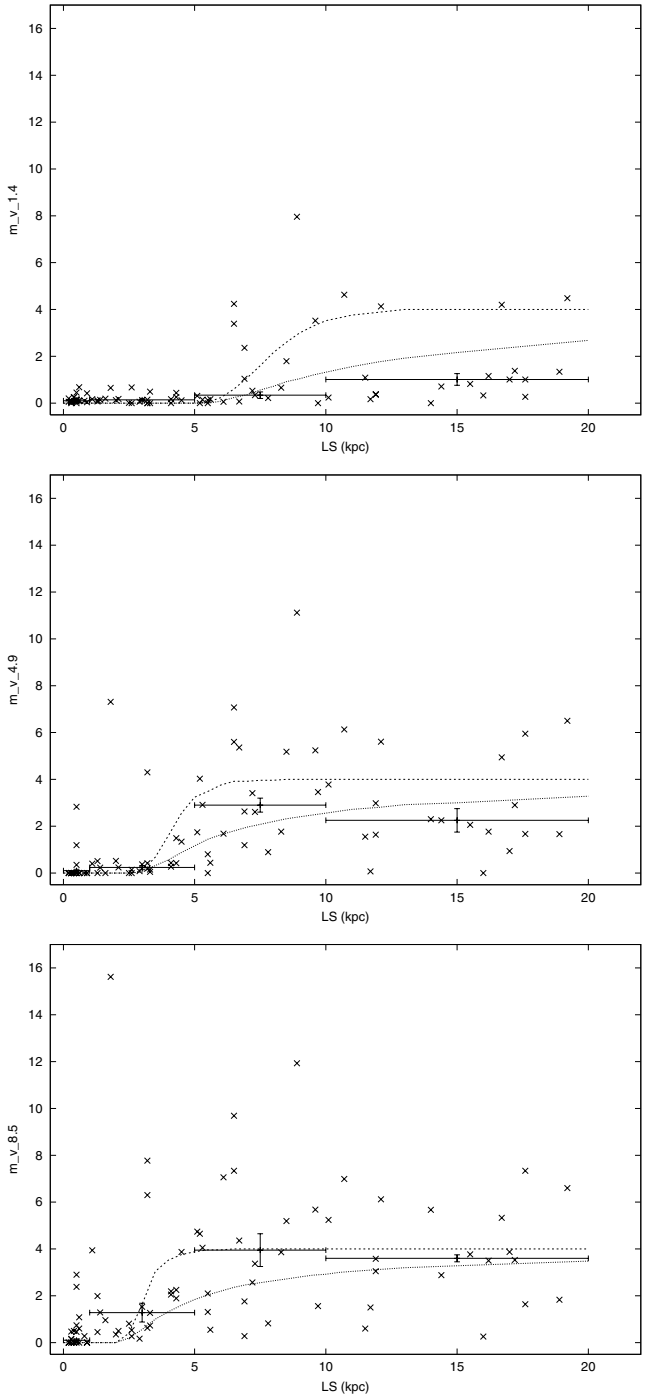

Fig. 8. Distribution of m_v as a function of LS, at 1.4, 4.9 and 8.5 GHz (from *top* to *bottom*). Median values are shown by horizontal segments. Two models, discussed in Sect. 5.4, are shown: the lower curve is for uniform brightness over the whole source extent; the upper curve is for a brightness distribution concentrated in the outermost thirds of the source extent.

is the result of a very strong frequency dependent depolarization, the *DP*s of the remaining half of the sources may not be representative of the class.

5. Discussion

5.1. Modelling the depolarization

A magnetized plasma interposed between the observer and the radio source can be responsible for the changes in the properties of the polarized emission. This plasma can be internal to the source, a foreground screen, or both. It is now generally believed that much of the Faraday Rotation and Depolarization take place in a foreground screen which is located in the vicinity of the radio emitting regions. The influence of such a "Faraday screen" on the depolarization characteristics of a radio source depends basically on the characteristics of the magnetized medium, such as inhomogeneities (often referred to as "cells"). Here we try to interpret the data using the two models by Burn (1966) and Tribble (1991). The latter, which is a more general treatment, reduces to the former in the case of very small "cells". In either model, the covering factor of the cells is assumed to be unity. Here we briefly summarize the characteristics of the two models.

Burn model

Burn (1966) assumes "cells" of identical size and discusses two extreme situations: *a)* the external screen is fully resolved by the observations ("cell" size comparable or larger than the observing beam); in this case the Faraday Depth $\Phi = \int n_e B_\parallel \mathrm{d}l$ is constant within the beam, no depolarization occurs, and the polarization angle rotates as: $\chi(\lambda) = \chi_0 + \lambda^2 RM$; *b)* the screen is totally unresolved ("cells" much smaller than the beam size). In the hypothesis that RM is randomly distributed with dispersion σ, the fractional polarization as a function of λ^2 is given by a Gaussian law:

$$m(\lambda) = m_0 \mathrm{e}^{-2\sigma^2\lambda^4}. \quad (1)$$

Observations have shown that Eq. (1) predicts too a low fractional polarization at long wavelengths (see e.g. Tribble 1991 and references therein).

Tribble model

The Tribble model also assumes that RM is randomly distributed with dispersion σ but, in addition, it assumes a distribution of the "cell" sizes. For a quadratic structure function of the RM the average squared fractional polarization follows the simple analytic expression:

$$\left\langle |m(\lambda)|^2 \right\rangle = m_0^2 \left[\frac{1 - \mathrm{e}^{-(s_0^2/2b^2 + 4\sigma^2\lambda^4)}}{1 + 8\sigma^2\lambda^4 b^2/s_0^2} + \mathrm{e}^{-(s_0^2/2b^2 + 4\sigma^2\lambda^4)} \right] \quad (2)$$

where s_0 is a characteristic scale which can be taken to represent the largest cell scale and b is the beam size of the observations. Note that now $m(\lambda)$ depends on both σ and s_0/b.

Particularly interesting is the so called "long wavelength" behaviour: when $4\sigma^2\lambda^4$ is very large and dominates, Eq. (2) reduces to:

$$m(\lambda) \approx m_0 \left[\frac{s_0/b}{2\sigma\lambda^2\sqrt{2}} \right] \quad (3)$$

and the fractional polarization decreases with λ^2 more slowly than in Eq. (1). Equation (3) depends on the ratio $(s_0/b)/\sigma$,

Table 4. Mean and median fractional polarization per interval of LS.

		Mean			Median		
LS (kpc)	N	$\langle m_v^{8.5} \rangle$	$\langle m_v^{4.9} \rangle$	$\langle m_v^{1.4} \rangle$	$m_v^{8.5}$	$m_v^{4.9}$	$m_v^{1.4}$
<1	22	0.44 ± 0.18	0.29 ± 0.15	0.17 ± 0.04	$0.10^{+0.10}_{-0.06}$	$0.10^{+0.06}_{-0.06}$	$0.10^{+0.03}_{-0.02}$
1–5	23	2.50 ± 0.80	0.80 ± 0.36	0.18 ± 0.04	$1.28^{+0.60}_{-0.40}$	$0.24^{+0.18}_{-0.08}$	$0.14^{+0.04}_{-0.04}$
5–10	20	4.2 ± 0.66	3.4 ± 0.60	1.48 ± 0.46	$3.95^{+0.50}_{-0.70}$	$2.9^{+0.70}_{-0.30}$	$0.34^{+0.60}_{-0.14}$
10–20	19	3.8 ± 0.50	2.8 ± 0.5	1.31 ± 0.37	$3.6^{+0.60}_{-0.15}$	$2.25^{+0.70}_{-0.50}$	$1.01^{+0.15}_{-0.25}$

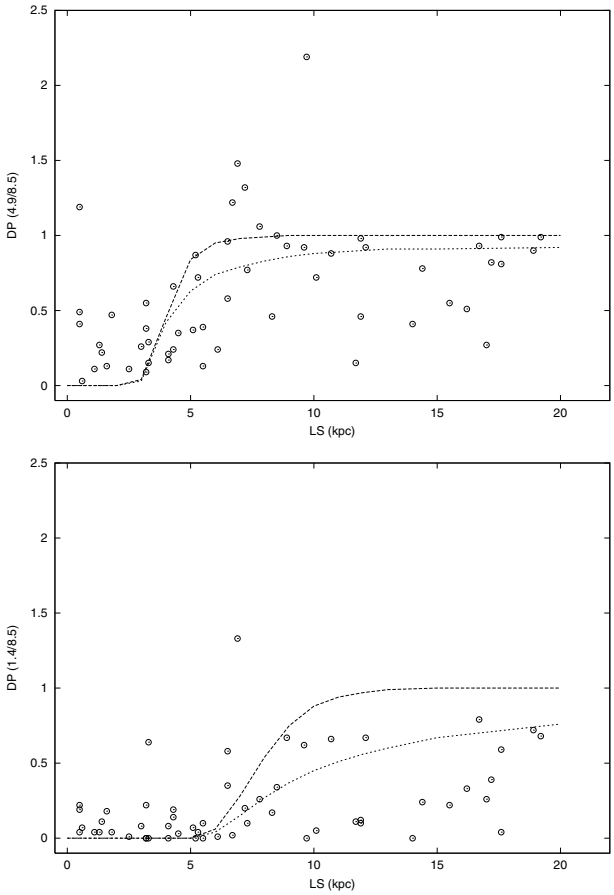

Fig. 9. Distribution of DP as a function of LS with the two models of Fig. 8. *Top*: 4.9–8.5 GHz; *bottom*: 1.4–8.5 GHz.

therefore the same "long wavelength" behaviour can be obtained with small s_0/b and small σ or proportionally larger s_0/b and σ. This degeneracy can only be broken if data at intermediate wavelengths and/or resolutions are available.

Equation (2) reproduces Burn's results for $b \to 0$ (screen totally resolved, $m(\lambda) \approx$ constant) and for $b \to \infty$ (screen totally unresolved, Eq. (2) tends to Eq. (1)).

5.2. Modeling the three-frequency depolarization of individual sources

A study made at three frequencies allows, in principle, discrimination between the two models of Burn (1966) and Tribble (1991) summarized in Sect. 5.1 and the derivation of the source Faraday Dispersion σ and of the "cell" scale parameter s_0/b. Note that for unresolved sources, as in our case, the source size itself determines the sampling beam (see Tribble 1991).

In thirty-eight sources of our sample m_v has $S/N \geq 4$ at both 8.5 and 4.9 GHz and in twenty-eight of them $m_v^{1.4}$ has $S/N \geq 3$. Note that the large majority of these sources have LS $\geq$ 5 kpc (Sect. 4.3). Such data quality is good enough to attempt a model-fitting of their fractional polarization, in spite of the very minimum number of measurements. In order to do this we first corrected $m_v^{1.4}$ for bandwidth depolarization using Fig. 23 of Condon et al. (1998). We have used the RM computed from the present data (mostly RM_3, Sect. 4.3). For the majority of the sources, the estimated $|RM|$ are $\lesssim$150 rad/m^2 and the corrections to $m_v^{1.4}$ are at most $\approx$30%. In five sources, instead, for which our RMs are $\geq$200 rad/m^2, the correction factors would be $\geq$2 (see, e.g., 0137+401 in Fig. 10) and probably somewhat uncertain (Sect. 4.4).

The results of the fits, reported in Table 6, can be summarized as follows:

- In nineteen sources the depolarization can be described by a Burn λ^2-Gaussian model without any need for a more complicated fit. Thirteen of these objects have a moderately small Faraday Dispersion ($\sigma \leq 50$ rad/m^2). The remaining six objects, strongly depolarized between 3.5 and 6 cm (8.5 and 4.9 GHz) and with $m_v^{1.4}$ compatible with zero ($S/N \lesssim 1$), require larger Faraday Dispersion ($\sigma \approx 200$ rad/m^2).
- In seven further sources with significant depolarization at the shortest wavelengths an acceptable fit has been obtained only with the Tribble model. As there is some degeneracy of the ratio $(s_0/b)/\sigma$ (Sect. 5.1), due to the poor frequency coverage, the solution for these models may be not unique. We have always taken the solution with the smallest acceptable σ and s_0/b. Also † 1343 + 386 is better fitted with the Tribble model (see below). In these fits the median value of s_0/b is $\approx$1.0.
- Five sources cannot be fitted even by the Tribble model because $m_v^{1.4}$ is too high with respect to the drop in polarization between 3.5 and 6 cm (see, e.g., 0228+409A in Fig. 10). For the source 1025+390B, $m_v^{1.4}$ is not available and the two high frequency data-points show an "inverted" behaviour in m_v, so no fit for this source is possible.
- Among those five sources mentioned earlier in which the correction for bandwidth depolarization at 20 cm is too uncertain, for two (0137+401 in Fig. 10 and 0930+389) the data are compatible with a small Faraday Dispersion ($\sigma \leq 20$ rad/m^2). The remaining three may require a Faraday Dispersion of a few hundred rad/m^2.

Table 5. Mean and Median depolarization per interval of LS.

		Mean		Median	
LS (kpc)	N	$\langle DP^5_8 \rangle$	$\langle DP^{1.4}_{8.5} \rangle$	$DP^{4.9}_{8.5}$	$DP^{1.4}_{8.5}$
1–5	23	0.34 ± 0.08	0.25 ± 0.11	$0.22^{+0.05}_{-0.03}$	$0.08^{+0.06}_{-0.04}$
5–10	20	0.80 ± 0.08	0.30 ± 0.08	$0.90^{+0.10}_{-0.10}$	$0.20^{+0.10}_{-0.10}$
10–20	19	0.67 ± 0.08	0.38 ± 0.08	$0.80^{+0.10}_{-0.10}$	$0.33^{+0.30}_{-0.11}$
>40	45	0.97 ± 0.05	0.64 ± 0.06	$0.90^{+0.06}_{-0.08}$	$0.66^{+0.10}_{-0.08}$

The data for LS > 40 kpc are from Klein et al. (2003).

Note that, with a moderate change in Faraday Dispersion, for sixteen out of the nineteen sources fitted by the Burn model, a Tribble model with $s_0/b \approx 1$ is also acceptable, while 0049+379, 1204+401 and 2322+403 require smaller values of s_0/b (see values in Table 6). The differences between the two depolarization models would appear only if measurements at intermediate wavelengths between 6 and 20 cm were available (see e.g. †1343+386). For homogeneity, we give in Table 6 the results of this second fit instead of those from the Burn model.

Table 6 therefore gives the 3-point fitted σ (observed and in the source frame – sf), s_0/b, and $m_0 = m(\lambda = 0)$, *always* from the Tribble model. For the sources initially fitted with the Burn model s_0/b is given within square brackets. For the six sources without a reliable three frequency fit and for those five with uncertain (large) correction for bandwidth depolarization at 1.4 GHz the Faraday Dispersion (in parenthesis) and m_0 are estimated using the two higher frequencies only. Faraday Dispersion in the source frame, σ_{sf}, are computed using the red-shift from Table A.1. For sources without red-shift $z = 1.05$ has been assumed and the computed σ_{sf} is given in square brackets.

Figure 11 shows the distribution of the Faraday Dispersion (both in the observer's frame, σ_{obs}, and in the source frame, σ_{sf}). The distribution of σ_{obs}, which is representative for sources with LS $\geq$ 5 kpc, shows a peak at $\sigma \leq 50$ (rad/m^2) and a long tail extending to a few hundred rad/m^2. It is in the tail that the sources unambiguously described by the Tribble model are found, since only for high Faraday Dispersions does the predicted long wavelength flattening of the depolarization curve occur within our wavelength range. Note that the exclusion of sources not meeting the selection criteria adopted to derive the parameters reported in Table 6 (e.g. less significant m^5_v or $m^{1.4}_v$) would produce a deficiency of high values σ_{obs} (see Sect. 5.3).

Figure 12 shows the distribution of the intrinsic fractional polarization values, m_0, given in Table 6. The median of the distribution is $m_0 = (4.0 \pm 1)\%$.

A check of the reliability of the above results is obtained from the ten sources for which the polarization is measured at 2.7 GHz by Klein et al. (2003). We obtain the following results:

– In five cases (0213+412, 0805+406, † 0809+404, 0955+390 and 1220+408) the 2.7 GHz data are consistent with the three frequency model, eventually with minor changes of the parameters (see, e.g., 0805+406 and 1220+408 in Fig. 10).
– In four cases (†0110+401, †0754+396, †1343+386 and 2304+377 in Fig. 10) the 2.7 GHz polarization is incompatible with the 3-point initial model, being significantly too low in the first three sources and too high in the latter. In the case of † 1343+386 a drastic change from the Burn model to the Tribble model allows a mediocre fit, and the latter model parameters are reported in Table 6. The tenth source († 0800+472, not shown) could not be fitted with either Burn or Tribble models, even with the addition of the 2.7 GHz data.

In the case of † 0754+396 (Fig. 10), the fractional polarization drops quickly in the interval $3.5 < \lambda < 11$ cm (the data at $\lambda \lesssim 11$ cm are well fitted by a λ^2-Gaussian with $\sigma = 45$ rad m^{-2}) and it then appears to remain roughly constant. There may be a simple explanation for this behaviour. The source (see the high resolution data in Table A.2) has two distinct components one of which does not depolarize between 8.5 and 4.9 GHz, while the other shows depolarization between these frequencies. It is then possible that the second component becomes totally depolarized at 2.7 GHz, while the other may remain polarized down to 1.4 GHz. This would explain the observed behavior. The polarized flux density measured at 1.4 GHz can in fact be totally accounted for by the component supposed to remain polarized. The behaviour of m_v vs. λ^2 for the source 2304+377, which we know is also double (Paper II), suggests a similar explanation, although we have no confirmation from the polarization structure, it being unresolved at our resolution. In passing we note that this explanation could apply also to the sources not fitted by either the Tribble or the Burn model, as these sources show asymmetries in depolarization. In addition, large spectral differences between the source components could conspire in such a way that at short and long wavelengths a different component dominates the polarization properties.

The last source, † 0110+401 (Fig. 10), shows an unusual behaviour. The fractional polarization drops by more than a factor of two at 11 cm (actually the data at $\lambda \leq 11$ cm are well fitted by a λ^2-Gaussian with $\sigma = 68$ rad m^{-2}) and then goes up at 20 cm, once more reaching the short wavelength value. This behaviour is what would be expected in the case of the beating of two components of similar polarized fluxes and Rotation Measures differing by some 60 rad/m^2. We have noted earlier (Sect. 4.3) that there are sources in which the components exhibit such behaviour. However, at our resolution the source is

Table 6. Depolarisation parameters.

	Name	σ_{obs}	σ_{sf}	s_0/b	$m_0(\%)$	Notes
	0003+387	250	1525	[1]	2.4	
†	0034+444	75	1080	[1]	3.2	
	0039+412	20	[85]	[1]	5.2	
	0049+379	296	2160	[0.5]	9.0	
†	0110+401	9	55	[1]	5.1	3
	0120+405	(140)	470		5.2	1
†	0123+402	100	[420]	[1]	4.7	
	0137+401	(≤12)	≤80		1.6	1
	0144+432	19	100	[1]	3.2	
	0213+412	60	140	1.0	3.1	4
	0222+422A	225	4560	1.5	3.6	
	0228+409A	(200)	[840]		3.5	2
	0254+406	10	50	[1]	1.7	
	0744+464	(200)	3080		4.7	1
†	0748+413B	215	[900]	1.1	17.2	
†	0754+396	11	110	[1]	11.5	3
†	0800+472	(100)	[420]		2.4	2
	0805+406	11.5	[50]	[1]	6.7	4
†	0809+404	250	600	0.9	4.4	4
	0930+389	(≤18)	≤210		2.9	1
	0951+422	(180)	1395		3.9	2
	0955+390	12	[50]	[1]	6.6	4
	1025+390B	??			∼2	2
†	1039+424	14	[60]	[1]	7.2	
†	1044+454	(190)	4940		8.3	1
†	1055+404A	11	[45]	[1]	5.8	
	1201+394	44	90	[1]	3.0	
	1204+401	30	280	[≤0.1]	4.9	
	1216+412	(200)	620		3.8	2
	1220+408	80	[500]	0.4	7.5	4
	1233+418	140	220	0.7	4.2	
†	1343+386	150	1210	1.7	3.0	5
	1350+432	(150)	1490		9.7	2
	1458+433	≈0	≈0	[1]	2.3	
	2304+377	270	530	1.2	3.2	3
	2311+469	13	40	[1]	5.5	
	2322+403	195	[820]	[≤0.2]	6.5	
	2348+450	300	1175	[1]	2.4	

Faraday dispersions (σ_{obs} and σ_{sf}) are in rad m^{-2}. Values in [ ] for s_0/b mark sources equally well fitted by Burn *and* Tribble models.
Notes:
1 = too a high RM to allow a reliable correction of $m_v^{1.4}$;
2 = no acceptable model;
3 = bad fit with the 2.7 GHz data;
4 = fair agreement with the 2.7 GHz data;
5 = change of model (see text).

extended and rather amorphous and thus at present, we do not have any direct evidence for the suggested explanation.

5.3. Faraday dispersion vs. red-shift

Pentericci et al. 2000, in a sample of 37 high red-shift radio galaxies (HzRG) found that the intrinsic (i.e. $z-$corrected) RMs can assume very high values and that at $z > 3$ ≈ 80% of the HzRGs have an intrinsic $RM > 1000$ rad/m^{-2}. In addition, using low-z radio galaxies from the literature, they find that the fraction of objects with $RM > 1000$ rad/m^{-2} systematically increases with red-shift and conclude that high-z objects are embedded in an intra-cluster environment denser than nearby radio galaxies. They exclude CSSs from their analysis on the premise that in these objects the RM is dominated by the effects of the host galaxy magnetized ISM.

Our results (Sect. 4.5) show that while for the smallest sources (LS $\lesssim$ 3 kpc) the ISM is very efficient in randomly rotating the polarization vector so as to depolarize the source completely, for the more extended sources the depolarization is not so strong. (see Sect. 5.4.1). This allows us to investigate the environment of CSSs as a function of red-shift for distances ≳1.5 kpc from the nucleus. Note that, in this case, we refer mainly to the Interstellar Medium, since CSSs are totally embedded in this.

The plot of the source-frame RMs vs. red-shift (Fig. 13) for those objects in Table 3 which have LS > 3 kpc gives a marginally significant correlation, with a ≈3% probability of being due to random fluctuations. We note that the uncertainty introduced in the determination of RM_3 by the $n_{1.4}\times180°$ ambiguities discussed in Sect. 4.3 may blur any existing correlation.

We then considered the Faraday Dispersion. In our sample there are fifty objects with LS ≳ 3 kpc of which thirty-four have a measured photometric or spectroscopic red-shift. For twenty-three of these we have already listed the Faraday Dispersion in Table 6. A further eight objects (0140+387, 0255+460, 0810+460B, 0856+406, 0935+428A, † 1136+420, 1143+456, 2349+410) had measurements of m_v^8 larger than 3 times the rms but non-detections of m_v^5 or $m_v^{1.4}$. For these we computed σ_{obs} from the two high frequencies, adopting for m_v^5 either the value reported in Table A.3 or 1-rms, whichever is the larger. Three remaining objects are not plotted: 0128+394 and 0701+392 have too low a value of m_v^8 and in addition, together with 1025+390B, have $DP_{8.5}^{4.9} > 1$, therefore their Faraday Dispersion cannot be computed. The sample is not complete since ≈32% of the objects more extended than 3 kpc do not have measured red-shifts. However, it can be considered representative of the class since bias is unlikely to be introduced in σ_{sf} by excluding objects without a measured red-shift.

The results are shown in Fig. 14 (left) where a trend of σ_{sf} with z is clearly visible: at $z < 1$ only "low" Faraday Dispersions are present while large values of are found only at high red-shifts. No data points were found in the quadrant [$z < 1$, $\sigma_{sf} > 1000$ rad/m^2]. A chi-square test for a contingency table gives a probability less than 0.5% that this effect is spurious. After removing the six objects with a photometric

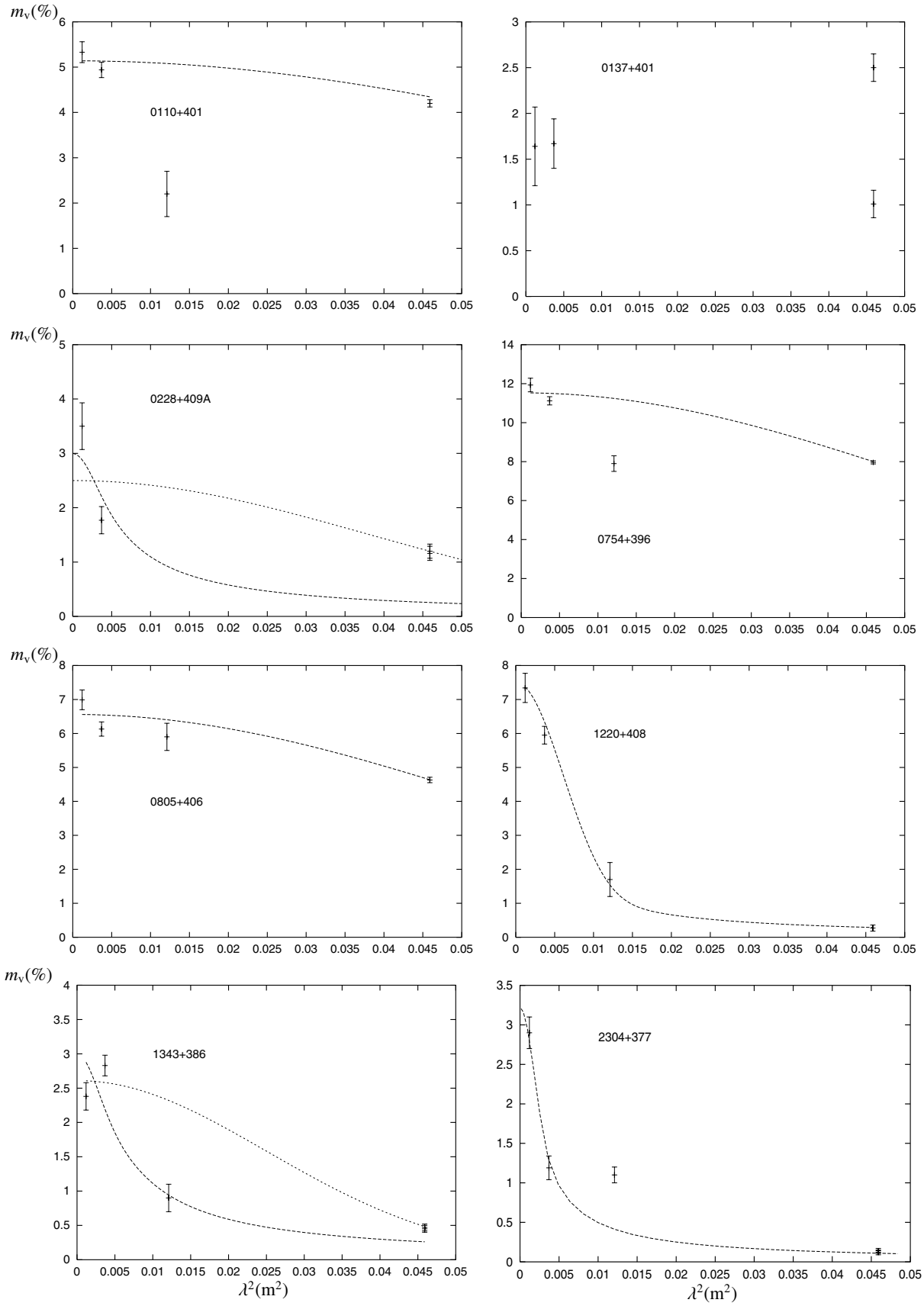

Fig. 10. Fits with the Burn and/or Tribble models for some of the sources discussed in the text. The data points at $\lambda = 0.11$ m ($\nu = 2.7$ GHz) are from Klein et al. (2003). The two values of $m_v^{1.4}$ (e.g. 0137+401) are the one given in the NVSS catalogue and the one corrected for bandwidth depolarization.

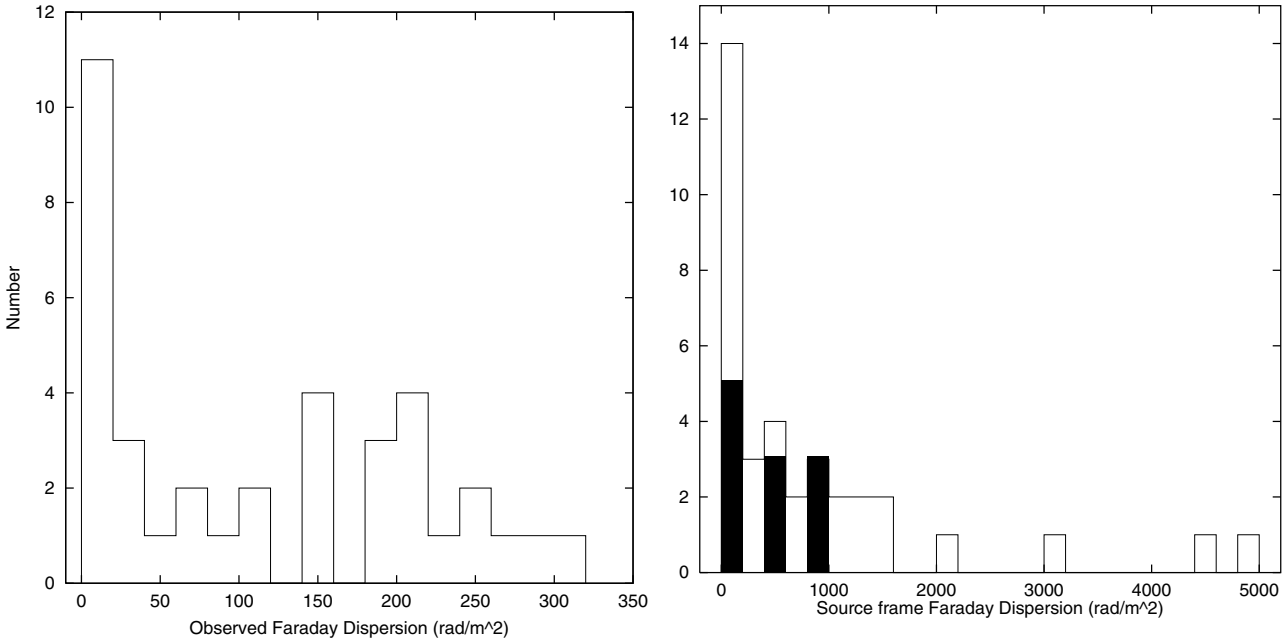

Fig. 11. Distribution of the Faraday Dispersions in the observer frame (*left*) and in the source frame (*right*). Dark bars indicate sources without red-shift for which $z = 1.05$ has been assumed.

(more uncertain) red-shift, the effect still remains significant at a 99% level.

An alternative way to show the dependence of σ_{sf} on z is given on the right side of Fig. 14, where we plot σ_{obs} vs. z. If σ_{sf} were independent of z we would expect an inverse proportionality between σ_{obs} and $(1 + z)^2$, which is not present. As an example we plot the curve expected as a function of z for $\sigma_{sf} = 900$ rad/m^2, which is the maximum intrinsic value found for $z < 1$. All data points corresponding to $z < 1$ are below the curve, while most of those corresponding to $z > 1$ are above this curve, indicating that their intrinsic Faraday Dispersion is larger.

A systematic effect able to remove data-points from the top-left quadrant (left panel) might be due to having considered only objects with a significant m_v^8. If these CSSs had $m_0 \approx 4\%$ (see Sect. 5.6) then too low a value of m_v^8 would imply a high Faraday Dispersion. The only two radio sources in such a situation, (0128+394 and 0701+392) however have $z > 1$ and therefore their exclusion does not affect the σ_{sf}/z plot.

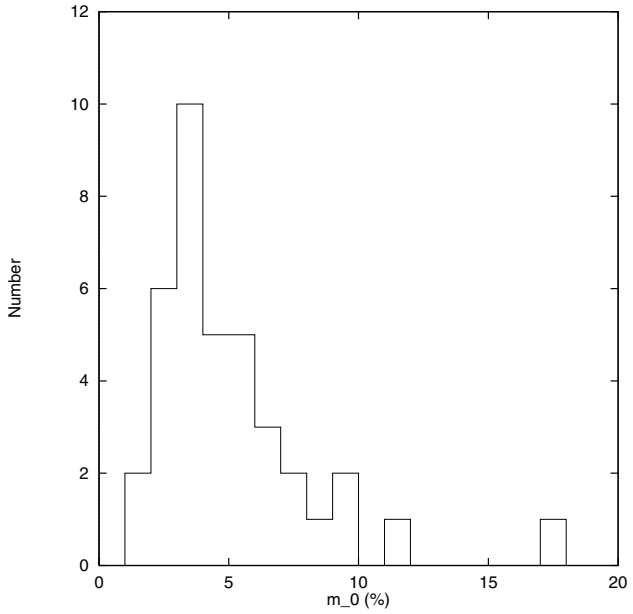

Fig. 12. Distribution of the intrinsic fractional polarisation m_0 (*low resolution*).

5.4. Modeling the linear size effect

5.4.1. A Faraday curtain

The dependence of the fractional polarization on linear size, found earlier by Cotton et al. (2003), is a major result obtained from the B3-CSS sample.

We have tried to model this result in terms of Faraday Depolarization occurring in the ambient medium of the radio source. We use a very simplified model which assumes that the Faraday Dispersion produced by the ambient gas has the following King-like distribution:

$$\sigma_{sf}(R) = \frac{F}{(1 + R^2/r_c^2)^{(6\gamma-1)/4}} \ \text{rad/m}^2 \qquad (4)$$

where r_c is the core radius, F is a parameter which contains the properties of the Faraday screen, γ is the usual parameter related to the radial distribution of the Faraday active medium and R is the distance of a region in the radio source from the line of sight to the center of the host galaxy.

We assume that the radio source axis is roughly perpendicular to the line of sight. This is consistent with the Unified Scheme models, since most sources of our sample are radio galaxies. The fractional polarization at the observed wavelength $\lambda_0 = \lambda_{source}(1 + z)$ and at a distance R from the galaxy core is computed, for simplicity, using the

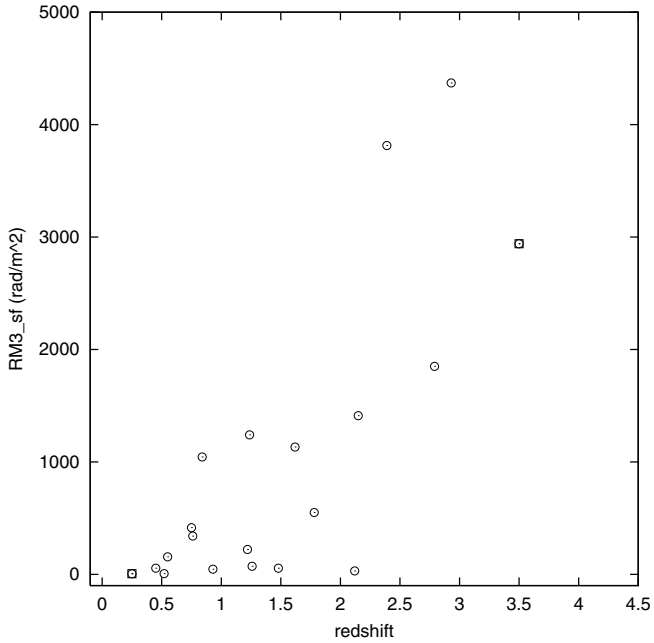

Fig. 13. Distribution of intrinsic RM_3 vs. red-shift; data-points in squares represent photometric red-shifts. See Sect. 4.3 for a discussion of uncertainties in RM_3.

Burn model (Eq. (1)). The use of the Tribble model produces minor differences which will be discussed later. In order to get the integrated $m_v(\lambda, \mathrm{LS})$ of the model, we have integrated $m_v(\lambda, R)$ along the source axis assuming different brightness distributions.

The wavelength dependent transition of depolarization in the range ≈3−6 kpc (Fig. 8) puts a number of constraints on the model parameters. We find that the more peaked the gas distribution (i.e. smaller r_c and larger γ), the sharper is the increase with LS of the fractional polarization and the closer to each other are, at the three frequencies, the LSs at which the jump occurs. Appropriate ranges of values for our data are:

$$\gamma \geq 1.3, \quad \text{and} \quad r_c < 1.0 \text{ kpc}$$

while the value of F is related to r_c and γ. The sharpness of the depolarization transition also depends on the brightness distribution of the source. For a uniform brightness distribution along the source axis, the integrated polarization increases smoothly with LS without sharp changes, while a sharper increase is obtained if the radio emission extends from the outer edges inward for only a fraction of the source radius, LS/2, (typically for no more than 50%).

In Fig. 8 two of the various models that we tried are shown superimposed on the distribution of m_v as a function of LS, at the three frequencies. In one model we have assumed that the source brightness is uniform over the whole source extent (lower curve), while in the second, the brightness distribution is concentrated in the outermost thirds. This second model is consistent with the structural information we have (see Paper I) as in half of the resolved sources the radio emission is concentrated in the outermost third of its extent. The model parameters are:

$$\gamma = 1.5, \quad r_c = 0.5 \text{ kpc}, \quad F \approx 1.5 \times 10^5 \text{ rad/m}^2$$

and, according to the distribution in Fig. 12, $m_0 = 4.0\%$. In order to correct the observed wavelengths to the source frame, we have used the median red-shift value of 1.05 (Sect. 2).

Models of this type account fairly well for the sharp increase in fractional polarization at ≈3−6 kpc, the change occurring first at 8.5 GHz, soon thereafter at 5 GHz and then at 1.4 GHz. There is a large dispersion around the models, which is a consequence of the dispersion in the values of m_0 (Fig. 12) and σ_{sf} (Fig. 11) and of the $\sigma_{sf} - z$ relation discussed in Sect. 5.3. At 8.5 GHz, the sources lying above the model lines do have $m_0 \geq 4\%$ whilst the opposite is true for those lying below the models. On the other hand, at 1.4 GHz it is the dispersion on σ_{sf} which plays the dominant role. At 5 GHz there are mixed contributions.

The effect of the spread in σ_{sf} on the dispersion of the data-points around the model is better seen in Fig. 9 which displays the depolarization ratios $DP^{4.9}_{8.5}$ and $DP^{1.4}_{8.5}$. These are independent of m_0 (and of its dispersion). This figure shows that the values of the parameters we have adopted in Eq. (4) properly describe the upper envelope of the distribution. The data-points close to it have values of σ_{sf} near the peak of the distribution of σ_{sf} displayed in Fig. 11. Those below the two model lines require larger values of σ_{sf}, typical of the tail of the σ_{sf} distribution. Most of the latter points are high red-shift objects (see Sect. 5.3). For these, a lower value of γ (≤1.0), namely a flatter distribution of the Faraday medium, is required to keep the same value of F.

Finally we note that in the small size range (LS ≤ 5 kpc) the models displayed in Fig. 8 predict zero fractional polarization, while several of the displayed points differ from zero. Whilst many more small sources with no significant polarization at any frequency cannot be displayed in these plots, we note that it is a characteristic of the Burn model that fractional polarization goes to zero at increasing Faraday dispersions. Had we used the Tribble model, the asymptotic values for $DP^{4.9}_{8.5}$ and for $DP^{1.4}_{8.5}$ at increasing σ_{sf} (decreasing LS) would have been ≈0.34 and 0.03 respectively, which would be in better agreement with the data.

5.4.2. The nature of the Faraday curtain

We consider two possibilities for the medium responsible of the depolarization effects.

i) A *smooth medium* with a King–like density distribution, $n_e(r) = n_0(1 + r^2/r_c^2)^{-3\beta/2}$, with a magnetic field intensity $B(r) = B_0(1 + r^2/r_c^2)^{-3\mu/2}$, where B_0 is the central magnetic field. In the case of equipartition between magnetic and thermal energy, $\mu = \beta/2$ for the isothermal case and $\mu = 5\beta/6$ for the adiabatic case. If B is frozen into the matter then $\mu = 2\beta/3$. The field orientation is assumed to be uniform within "cells" of size d_c and to change randomly from cell to cell, producing a Gaussian distribution of Faraday rotation (Sect. 5.1). In this model (see, e.g. Dolag et al. 2001), the Faraday dispersion is given by Eq. (4) with

$$F = KB_0 n_0 r_c^{1/2} d_c^{1/2} \quad \text{and} \quad \gamma = \beta + \mu$$

K is a quantity slightly dependent on γ (≈300 for $\gamma = 1.5$), B_0 and n_0 are measured in μG and cm^{-3} respectively and d_c and r_c in kpc.

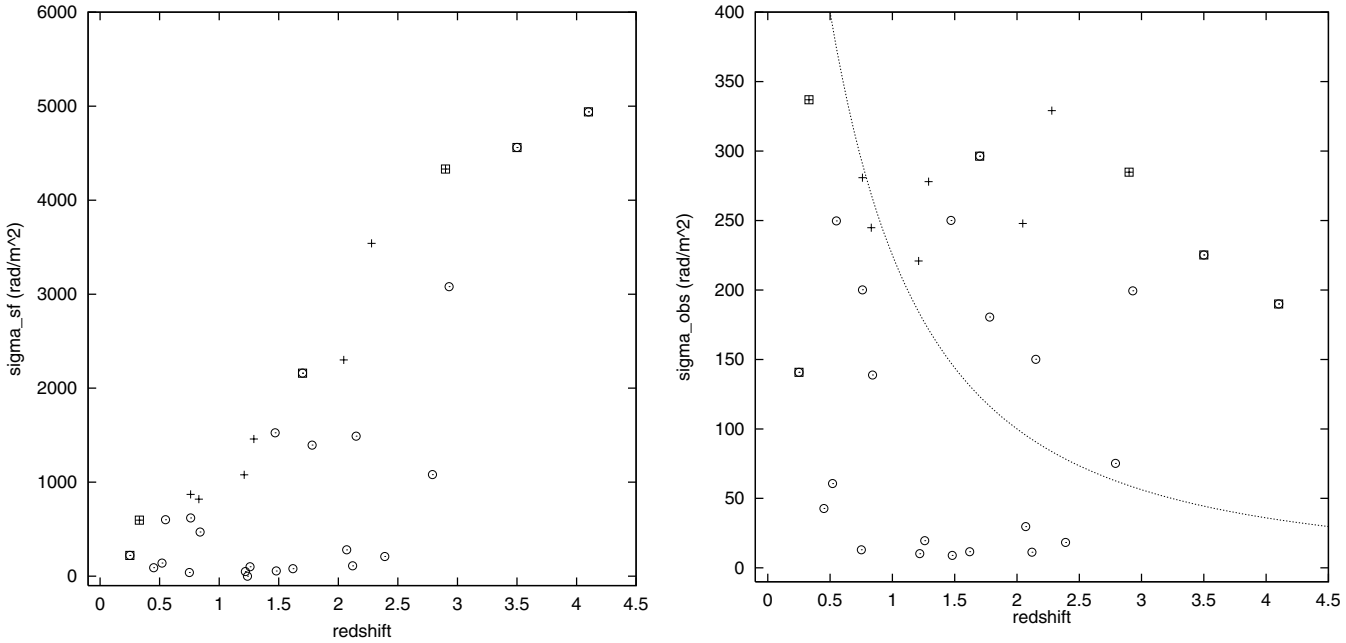

Fig. 14. Distribution vs. red-shift of the intrinsic (*left*) and of the observed (*right*) Faraday Dispersion. In both figures a *circle* marks the objects from Table 6; a *plus* sources with a more uncertain Faraday Dispersion (see text); a *square* photometric red-shifts. The curve on the right panel represents the expected $\sigma_{\rm obs}$ as a function of z for $\sigma_{\rm sf} = 900$ rad/m^2.

In order to disentangle B_0, n_0 and $d_{\rm c}$ from each other, additional assumptions are required. For instance, if we assume that thermal and magnetic energy are roughly in equipartition, as discussed by Rees (1987), assuming $T \approx 10^7$ K for the medium, $r_{\rm c} = 0.5$ kpc, $\gamma = 1.5$ and $F = 1.5 \times 10^5$, we get the following values:

$$n_0 \approx 1 \times (d_{\rm c})^{-1/3} \qquad B_0 \approx 280 \times (d_{\rm c})^{-1/6}.$$

The dependence of B_0 and n_0 on the cell size $d_{\rm c}$ is rather weak, so that in the context of the model, their values are reasonably fixed. We know nothing about $d_{\rm c}$ except that it has to be small compared with the sizes of the smallest sources in order to produce the observed strong depolarization, which constrains it to a size less than a few tens of parsec.

ii) A *clumpy medium* of magnetized clouds of size $d_{\rm cl}$ and filling factor f_0, whose space density decreases as $N_{\rm cl} = N_{0,\rm cl}(1 + r^2/r_{\rm c}^2)^{-3\gamma}$, with $N_{0,\rm cl} = f_0 d_{\rm cl}^{-3}$. In this case it is easily shown that the Faraday dispersion is given again by Eq. (4), with $F = KB_{\rm cl}n_{\rm cl}(f_0 r_{\rm c} d_{\rm cl})^{1/2}$.

If we assume that these clouds are those emitting the Narrow Lines, taking fiducial values of $n_0 = 10^4$ atoms cm^{-3} and $f_0 = 10^{-4}$, to produce $F \approx 1.5 \times 10^5$ we need:

$$B_{\rm cl} \approx 220 \times d_{\rm cl}({\rm pc})^{-0.5}\ \mu{\rm G}.$$

Assuming that the magnetic field pressure does not exceed the thermal pressure, namely that $B_{\rm cl} \leq 10^3\ \mu$G, we get that $d_{\rm cl} \geq 0.05$ pc, in agreement with independent spectroscopic estimates (e.g. Peterson 1997). However, in order that the *NLR* be an effective depolarizer it is required that the covering factor be close to unity, which implies, on average, a few clouds at least along the line of sight. The number of clouds along the line of sight is given by:

$$N_{\rm cl,los}(R) = \frac{f_0 r_{\rm c}}{d_{\rm cl}[1 + (R/r_{\rm c})^2]^{3\gamma - 0.5}}$$

with covering factor $\quad {\rm cf(R)} = 1 - {\rm e}^{-N_{\rm cl,los}(R)}$.

With the above quoted values for f_0, $d_{\rm cl}$ and $r_{\rm c} \leq 1$ kpc, $N_{\rm cl,los}$ is close to unity within the core radius and soon becomes exceedingly small for $R/r_{\rm c} \geq 1$, the covering factor rapidly approaching zero.

Alternatively we may assume that the *NL* clouds are distributed in a sheath around the lobes, as suggested by HST observations (e.g. de Vries et al. 1999; Axon et al. 2000), being produced by shocks driven by the lobe expansion (see, e.g., Bicknell et al. 1997). In this case, the filling factor in the sheath is certainly large, increasing the covering factor, which however, according to the above equations, still drops too fast for $R/r_{\rm c} \geq 1$.

In conclusion, the *NL* clouds alone do not seem the best candidates for depolarization. However we may speculate that they play a role at $R \leq r_{\rm c}$, while for $R \geq r_{\rm c}$ the smooth medium takes over.

5.5. Rotation and depolarization

In Sect. 4.4 (Fig. 6) we have shown that there is some correlation between the rotation angle $\Delta\chi_{8.5}^{4.9}$ and the depolarization ratio. The Rotation Measures we have derived in Sect. 4.3 are not too different from the Rotation Measures required by the observed depolarization. Furthermore, we have found that in a large fraction of sources the rotation angle seems to follow the λ^2 law down to 1.4 GHz.

These findings are somewhat unexpected in models for the Faraday screen characterised by cells much smaller than the source size and a randomly oriented magnetic field. In these cases, one does not expect much global Faraday rotation nor the angle to change with λ^2 over a broad wavelength range.

It appears that our findings require more sophisticated models which include cells with a broad range of sizes such that the small ones depolarize the radiation while the largest ones produce coherent rotation of the polarization angle. As there is no way to develop an analytic model of the expected *RM* for Faraday screens with a spectrum of cell sizes, numerical simulations need to be used, as in Murgia et al. (2004). We plan to use this approach in future work.

5.6. Intrinsic fractional polarization

According to Table 6 and Fig. 12, the intrinsic degree of polarization of CSSs with 5 < LS(kpc) < 20 has a median value ≈4%, extending up to ≈15%. Recently Ricci et al. (2004) have observed in polarization at 18.5 GHz a sample of 258 radio sources from the Kühr et al. (1981) 1 Jy sample using the Australian Telescope Compact Array. Of these, 71 sources have a steep spectrum and are unresolved at their resolution (15.6 arcsec), therefore they are likely to be mostly CSSs/GPSs. The median fractional polarization at 18.5 GHz of this subsample is $\approx 4.8^{+2}_{-1}\%$. Given the high observing frequency this can be taken as a good estimate of m_0 and agrees fairly well with our measurement.

It is interesting to compare these figures with the corresponding ones for radio sources of much larger size, to see if there are any differences between the two populations. Unfortunately, to our knowledge, there are not many samples of sources for which unbiased polarization data are available. We have chosen two samples of large size radio sources to be compared with ours.

The first sample is that of Klein et al. (2003). As it was originally selected at 10.5 GHz, this sample is biased in favour of sources strongly polarized at that frequency. Nevertheless the authors stress that from their data an unbiased sample of 208 B3−VLA sources can be defined, for which the fractional polarization at 10.5 GHz is known without biases down to ≈2%. We have extracted from this a sub-sample of 90 sources with LS ≥ 40 kpc and have examined its fractional polarization distribution at 10.5 GHz. A third of the sources have $m_{\rm v}^{10.5} \geq 5\%$, with values extending up to ≈15%. These figures are similar to those of our sample in the range 5 < LS(kpc) < 20. However the median value, $m_{\rm v}^{10.5} \approx 2\%$, is significantly lower than ours. It is unclear at the moment if this difference is real or if it is due to some unknown selection effect.

For the second comparison we have taken the sample of sources from Garrington et al. (1991), and from their data we have computed the integrated polarization at 5 GHz. Their distribution of the $m_{\rm v}^5$ has a median around 5.5%, slightly larger than our median value of ≈4%. However we note that their sample is not complete and it is likely that it is biased in favour of polarized sources. On the other hand, $m_{\rm v}^5$ may underestimate the intrinsic polarization. We suspect that the first bias likely plays a greater role.

Although these comparisons are, for different reasons, somewhat uncertain, we tend to believe that our *large* CSSs do not differ significantly from their much bigger cousins as far as the intrinsic fractional polarization is concerned. This, in turn, implies that the order of the source magnetic field has already reached a maximum at sizes ≈5−10 kpc.

5.7. Asymmetries in rotation measure and depolarization

We have pointed out that in several of the resolved sources, the components show asymmetries in rotation angle or depolarization or both. Recently Saikia & Gupta (2003) have also shown evidence for large polarization asymmetries in CSSs. According to our models for depolarization, in which the depolarization seems better accounted for by an external smooth medium, one would be led to ascribe the above asymmetries to the Laing-Garrington effect (Laing 1988; Garrington et al. 1988). The less depolarized (or less Faraday rotated) source component would be the one approaching us, the one with the greater arm length, and the one with a bright Doppler boosted jet, while the more depolarized (or Faraday rotated) one would be the receding shorter one and the one with a fainter jet (if any).

However, it is known that in a number of cases it is found that the jetted lobe is shorter than the other. Therefore, an alternative scenario has been suggested in which the depolarizing medium is not spherically symmetric and the two lobes experience in their expansion significantly different gas densities (see e.g. Thomasson et al. 2003; Junor et al. 1999). In this scenario the more depolarized (or Faraday rotated) lobe would then be the one expanding through the denser gas and would be more slowed down. Therefore, it would still be the closer to the core but no relation with the jet sidedness is necessarily expected. Saikia & Gupta (2003) discuss the propagation of jets in an asymmetric environment, which they suggest to be the result of infall of interstellar material into the central kpc region caused by the interaction or merger with a companion galaxy. Our data do not allow us to test the two alternatives as in the majority of cases we have not yet detected the cores and have not enough resolution to see which is the jetted lobe.

5.8. Orientation of the magnetic field

We have investigated the orientation of the magnetic field, in the whole source and in the individual components, with respect to the overall source orientation. For this purpose we have examined the distribution of the absolute values of the difference between the polarization angle at 8.5 GHz, χ_8, (assumed to be approximately the intrinsic orientation of $\boldsymbol{E}$ vector) and the source major axis position angle (PA). Only source/components with $m_{\rm v}^8 > 3$ rms have been used.

This distribution (not shown) provides a mild indication that large angles of $\boldsymbol{E}$ vector with respect to the source major axis may be preferred (i.e. the magnetic field seems to be

preferentially oriented parallel to the source axis). This is similar to what found for large size sources from the data of Garrington et al. (1991), where, using the integrated polarization angle at 4.9 GHz, χ_5, it is found that ~70% of the objects show this behaviour. Nevertheless statistical tests show that in our case the observed distributions is consistent with a flat distribution at a ≈80% confidence level. No difference is found between the smaller and the larger sources in the sample.

6. Conclusions

The main results of this paper are the following:

1) Integrated polarized flux is detected at one or more frequencies in ≥50% of sources.
2) The fractional polarization depends significantly on the wavelength, implying that strong Faraday effects are present. Moreover, at each frequency it depends strongly on the size of the sources. Those smaller than ≈3−5 kpc are either unpolarized at all three frequencies or strongly depolarized.
3) The median level of fractional polarization at $\lambda = 0$, for sources larger than 5 kpc, is $m_0 \approx 4\%$, although with a large scatter.
4) In ≥50% of cases, the position angle of the integrated polarization follows the λ^2 law from 3.5 to 20 cm (8.5 to 1.4 GHz). The observed Rotation Measures, corrected for the Galactic rotation, are up to few hundreds rad/m^2. When correcting for the $(1+z)^2$ factor, we find that ≈20% of the sources have intrinsic Rotation Measures in excess of 1000 rad/m^2.
5) The depolarisation is statistically correlated with the polarization rotation angle between 8.5 and 4.9 GHz.
6) The integrated fractional polarization as a function of our three wavelengths shows a variety of behaviours in individual sources. In most cases, the depolarization is described by the Burn or by the Tribble model. However, in those few cases were a fourth polarization measure (at 2.7 GHz from the literature) is available, in about half of the cases the initial fit is not supported. This emphasizes the need for a good wavelength coverage for such analyses.
7) In a number of sources resolved at 8.5 and 4.9 GHz, the components show asymmetries in depolarization and rotation angle. Depolarization and rotation angle are statistically correlated. These asymmetries are best interpreted as the effect of large scale inhomogeneities in the external depolarizing medium. Asymmetries in the intrinsic degree of polarisation are also present.
8) The dependence of depolarization on source linear size is roughly accounted for by a simple model which assumes a smooth distribution of the ambient depolarizing medium. The central density and magnetic field are determined to be $n_0 \approx 1$ cm^{-3} and $B_0 \approx 300$ μG. The contribution to depolarization from the *NLR* clouds seems less important.
9) Rotation Measure and Faraday Dispersion increase with red-shift, suggesting that the medium may be denser at high z.
10) The intrinsic fractional polarization of the *large* CSSs does not differ significantly from that of the ordinary extended radio sources, implying that the order of the source magnetic field has already reached a maximum at sizes ≈5−10 kpc.

Acknowledgements. We thank the meticulous anonymous referee for the numeorus very detailed comments which greatly helped in improving the paper's style. This work has been partially supported by the Italian MIUR under grant COFIN–2002–02–8118. The VLA is operated by the US National Radio astronomy Observatory which is operated by Associated Universities, Inc., under cooperative agreement with the National Science Foundation.

References

Axon, D. J., Capetti, A., Fanti, R., et al. 2000, AJ, 120, 2284
Bicknell, G. V., Dopita, M. A., & O'Dea, C. P. 1997, ApJ, 485, 112
Burn, B. F. 1966, MNRAS, 133, 67
Condon, J. J., Cotton, W. D., Greisen, E. W., et al. 1998, AJ, 115, 1693
Cotton, W. D., Dallacasa, D., Fanti, C., et al. 2003, Proc. of the 3rd International Workshop on Compact Steep Spectrum and Gigahertz-Peaked Spectrum Radio Sources PASA, 20, 12
Dallacasa, D., Fanti, C., Giacintucci, S., et al. 2002, A&A (Paper III)
Dallacasa, D., Tinti, S., Fanti, C., et al. 2002, A&A (Paper II)
de Vries, W. H., O'Dea, C. P., & Baum, S. A. 1999, ApJ, 526, 27
Dolag, K., Schindler, S., Govoni, F., & Feretto, L. 2001, A&A, 378, 777
Fanti, C., Fanti, R., Dallacasa, D., et al. 1995, A&A, 302, 317
Fanti, C., Pozzi, F., Dallacasa, D., et al. 2001, A&A, 369, 380 (Paper I)
Garrington, S. T., Leahy, J. P., Conway, R. G., & Laing, R. A. 1988, Nature, 331, 147
Garrington, S. T., Conway, R. G., & Leahy, J. P. 1991, MNRAS, 250, 171
Junor, W., Salter, C. J., Saikia, D. J., Mantovani, F., & Peck, A. B. 1999, MNRAS, 308, 955
Klein, U., Mack, K.-H., Gregorini, L., & Vigotti, M. 2003, A&A, 406, 579
Kühr, H., Witzel, A., Pauliny-Toth, I. I. k., & Nauber, U. 1981, A&AS, 45, 367
Laing, R. A. 1988, Nature, 331, 149
Murgia, M., Govoni, F., Feretti, L., et al. 2004, A&A, 424, 429
O'Dea, C. P. 1998, PASP, 110, 493
Orienti, M., Dallacasa, D., Fanti, C., et al. 2004, A&A, 426, 463 (Paper V)
Peterson, B. M. 1997, An Introduction to Active Galactic Nuclei (Cambridge University Press), 102
Pentericci, L., Van Reeven, W., Carilli, C. L., Röttgering, H. J. A., & Miley, G. K. 2000, A&AS, 145, 121
Readhead, A. C. S., Taylor, G. B., Xu, W., et al. 1996 ApJ, 460, 634
Rees, M. J. 1987, MNRAS, 228, 47p
Ricci, R., Prandoni, I., Gruppioni, C., Sault, R. J., & De Zotti, G. 2004, A&A, 415, 549
Saikia, D. J., Jeyakumar, S., Salter, C. J., et al. 2001, MNRAS, 321, 37
Saikia, D. J., Thomasson, P., Spencer, R. E., et al. 2002, A&A, 391, 149
Saikia, D. J., & Gupta, N. 2003, A&A, 405, 499
Simmons, J. F. L., & Stewart, B. G. 1985, A&A, 142, 100
Thomasson, P., Saikia, D. J., & Muxlow, T. W. B. 2003, MNRAS, 341, 91
Tribble, P. C. 1991, MNRAS, 250, 726
Vigotti, M., Grueff, G., Perley, R., et al. 1989, AJ, 98, 419
Wardle, J. F. C., & Kronberg, P. P. 1974, 194, 249

Online Material

Appendix A:

Table A.1. The B3-VLA sample of CSS.

Name	Id	z	*LAS* (arcsec)	*LLS* (kpc h^{-1})	Morph.		Name	Id	z	*LAS* (arcsec)	*LLS* (kpc h^{-1})	Morph.	
0003+387	G	1.47	1.3	5.5	MSO		1025+390B	G	0.361	~3.2	~9.7	MSO	
0034+444	G	2.79	3.2	11.9	MSO?	†	1027+392	E		~1.6	[~6.9]	?	†
0039+373	G	1.006	0.1	0.5	CSO		1039+424	E		~1.5	[~6.5]	?	†
0039+391	G	1.01	0.34	1.6	MSO		1044+454	G	4.1 K	1.0	3.2	MSO?	†
0039+398	E		3.7	[16]	MSO		1049+384	G	1.018	0.1	0.9	CSO	
0039+412	E		2.0	[8.5]	MSO		1055+404A	E		2.8	[12.1]	fcJ	†
0041+425	E		1.0	[4.1]	MSO		1128+455	G	0.40	~0.9	~2.9	MSO	
0049+379	G	1.7 K	1.45	6.1	MSO		1133+432	E		0.07	[0.2]	CSO	
0110+401	Q	1.479	~3.9	~16.7	?	†	1136+383	E		0.05	[0.3]	CSO	
0120+405	G	0.84	2.4	10.1	MSO		1136+420	G	0.829	1.0	4.3	MSO?	†
0123+402	G[a]		1.1	[5.2]	MSO?	†	1141+466	G	0.06	8.1	6.3	MSO	
0128+394	G	1.6 K	2.7	11.5	MSO		1143+456	G	0.762	0.8	3.3	MSO	
0137+401	Q	1.62	4.2	17.6	MSO		1157+460	G	0.742	~0.8	~2.5	MSO	
0140+387	G	2.9 K	0.7	4.1	MSO		1159+395	G	2.37	0.05	0.3	CSO	
0144+432	Q	1.26	~4.0	~17.2	MSO		1201+394	G	0.445	2.1	7.2	MSO	
0147+400	E		0.1	[0.4]	CSO		1204+401	G	2.066	1.6	6.7	MSO	
0213+412	G	0.515	2.0	7.3	MSO		1212+380	G	1.5 K	0.3	2.0	MSO	
0222+422A	G	3.5 K	3.4	11.9	MSO		1216+402	G	0.756	3.8	15.5	MSO	
0228+409A	E		3.8	[16.2]	MSO		1217+427	E		2.7	[11.7]	MSO	
0254+406	G	1.224	~4.5	~18.9	MSO		1220+408	G[b]		4.1	[17.6]	MSO	
0255+460	Q	1.21	0.66	3.2	MSO		1225+442	G	0.22 R	0.2	0.9	CSO	
0701+392	Q	1.238	1.8	7.8	MSO		1233+418	G	0.25 R	~2.2	~5.3	MSO	
0703+468	E		0.08	[0.3]	CSO		1241+411	G	0.259	~1.0	~2.6	MSO	
0722+393A	E		0.25	[1.3]	MSO		1242+410	Q	0.811	0.04	0.3	CSO	
0729+437	E		1.3	[5.6]	MSO		1314+453A	G	1.544	0.16	0.8	CSO	
0744+464	G	2.926	1.4	5.1	MSO		1340+439	E		0.07	[0.6]	CSO	
0748+413B	E		~0.4	[~1.8]	?	†	1343+386	Q	1.844	0.11	0.5	CSO?	†
0754+396	G	2.119	~2.2	~8.9	scJ	†	1350+432	G	2.149	1.6	6.5	MSO	
0800+472	E		~1.0	[~4.3]	scJ?	†	1432+428B	E		0.04	[0.2]	CSO	
0805+406	E		~2.5	[~10.7]	MSO		1441+409	E		0.1	[0.6]	CSO	
0809+404	G	0.551	1.2	4.5	MSO?	†	1445+410	G	0.18	8.1	15.7	MSO	
0810+460B	G	0.33 R	0.63	3.0	MSO		1449+421	E		0.08	[0.5]	CSO	
0814+441	E		4.0	[17.0]	MSO		1458+433	G	0.927	1.6	6.9	MSO	
0822+394	G	1.18	0.05	0.3	CSO		2301+443	G	1.7 K	0.5	2.1	MSO	
0840+424A	E		0.08	[0.6]	CSO		2302+402	E		0.6	[2.6]	MSO	
0856+406	G	2.28	0.8	3.2	MSO		2304+377	G	0.40 R	0.1	0.5	CSO	
0902+416	E		0.34	[1.4]	MSO		2311+469	Q	0.745	2.4	9.6	MSO	
0930+389	G	2.395	3.7	14.4	MSO		2322+403	E		3.2	[14.0]	MSO	
0935+428A	G	1.291	1.3	5.5	MSO		2330+402	E		0.07	[0.4]	CSO	
0951+422	Q	1.783	2.0	8.3	MSO		2348+450	G	0.978	0.2	1.3	MSO	
0955+390	E		~4.8	[~19.2]	MSO		2349+410	Q	2.046	1.2	3.3	MSO	
1007+422	E		0.13	[1.1]	MSO		2358+406	E		0.08	[0.5]	CSO	
1008+423	E		0.05	[0.5]	CSO								
1014+392	G	0.206	6.1	13.2	MSO								
1016+443	G	0.33 R	0.11	0.4	CSO								

Id as follows: G = galaxy; Q = quasar; E = empty field; [a] $m_R = 23.8$; [b] $m_R = 23.2$ no z available.
[*LLS*] computed assuming $z = 1.05$ for sources without z (see Paper I).
Morphological Classification (last column)
– *MSO* and *CSO*: see definition in Sect. 2;
– *scJ* or *fcJ*: Jet with a steep or a flat spectrum "head";
– † asymmetric or uncertain morphology.

Table A.2. *High Resolution* data (errors in parenthesis).

		8.5 GHz						4.9 GHz					
Name	c	S_I (mJy)		m_v(%)		χ(°)		S_I (mJy)		m_v(%)		χ(°)	
0003+387	N	22.71	(0.14)	2.72	(0.52)	80.4	(5.8)	53.45	(0.14)	0.95	(0.2)	78.5	(7.6)
	S	22.83	(0.15)	5.33	(0.56)	16.6	(3.6)	51.92	(0.15)	2.62	(0.3)	−3.0	(3.6)
†0034+444	N	84.12	(0.13)	3.59	(0.24)	20.6	(2.7)	164.49	(0.13)	3.26	(0.2)	34.7	(2.5)
	C1	4.75	(0.09)	2.22	(1.60)	62.9	(16.3)	7.88	(0.09)	1.61	(1.0)	71.3	(14.6)
	C2	1.87	(0.08)	12.35	(3.56)	76.1	(8.1)	5.10	(0.08)	4.22	(1.3)	68.3	(8.7)
	S	1.42	(0.08)	18.22	(4.62)	87.2	(7.3)	6.02	(0.08)	0.00	(1.1)	88.4	(28.3)
0039+398	E	5.40	(0.12)	3.78	(1.72)	−31.6	(12.0)	11.10	(0.12)	1.83	(0.8)	−76.5	(12.1)
	W	112.41	(0.17)	0.43	(0.23)	74.8	(13.7)	214.55	(0.17)	0.00	(0.2)	−32.2	(72.6)
0039+412	N	51.57	(0.15)	6.60	(0.30)	−81.5	(2.4)	90.05	(0.15)	6.04	(0.2)	82.1	(2.2)
	C	17.03	(0.14)	3.36	(0.69)	−84.0	(6.2)	26.21	(0.14)	3.25	(0.5)	88.6	(4.5)
	S	7.70	(0.14)	4.06	(1.46)	−35.1	(9.9)	14.80	(0.14)	0.88	(0.8)	42.5	(19.2)
0041+425	N	26.60	(0.10)	4.57	(0.36)	62.3	(3.0)	53.70	(0.10)	0.74	(0.2)	37.9	(8.2)
	S	48.00	(0.10)	1.24	(0.26)	−85.0	(6.2)	88.50	(0.10)	0.00	(0.2)	22.4	(31.4)
0049+379	N	56.71	(0.16)	8.71	(0.31)	−17.0	(2.2)	124.62	(0.16)	2.03	(0.2)	12.6	(3.3)
	S	19.68	(0.15)	2.24	(0.65)	−18.7	(8.2)	50.21	(0.15)	1.01	(0.3)	−7.8	(8.0)
0120+405	E	68.05	(0.17)	7.64	(0.29)	51.6	(2.3)	133.79	(0.17)	5.27	(0.2)	6.7	(2.2)
	W	19.73	(0.13)	2.99	(0.57)	−35.2	(5.7)	35.48	(0.13)	4.19	(0.3)	−53.9	(3.0)
†0123+402	N	1.57	(0.10)	8.18	(5.12)	−46.7	(15.2)	2.64	(0.10)	4.40	(3.0)	−67.3	(16.3)
	C	18.46	(0.11)	9.31	(0.51)	78.4	2.5)	37.15	(0.11)	7.44	(0.3)	59.7	(2.3)
	S	18.09	(0.12)	0.62	(0.58)	54.2	(20.1)	34.94	(0.12)	1.11	(0.3)	38.2	(8.2)
0128+394	N	21.88	(0.14)	2.32	(0.53)	−51.8	(6.7)	44.53	(0.14)	1.62	(0.3)	−77.2	(5.3)
	S	17.89	(0.16)	1.06	(0.73)	41.9	(16.3)	36.55	(0.16)	1.49	(0.4)	73.8	(7.2)
0137+401	N	9.16	(0.14)	6.86	(1.22)	5.9	(5.4)	19.94	(0.14)	7.41	(0.6)	11.3	(3.0)
	C1	26.58	(0.15)	3.36	(0.49)	−65.0	(4.6)	39.12	(0.15)	2.39	(0.3)	−72.2	(4.5)
	C2	12.33	(0.14)	9.80	(0.90)	86.1	(3.3)	22.43	(0.14)	4.92	(0.5)	68.0	(3.5)
	S	7.61	(0.11)	8.04	(1.13)	33.8	(4.4)	13.55	(0.11)	6.20	(0.6)	36.3	(3.6)
0140+387	N	15.96	(0.13)	2.36	(0.69)	0.1	(8.2)	41.61	(0.13)	0.17	(0.3)	13.0	(25.5)
	S	13.73	(0.13)	3.47	(0.79)	−44.4	(6.6)	35.53	(0.13)	0.37	(0.3)	38.4	(19.0)
0144+432	N	19.84	(0.15)	11.43	(0.65)	−4.3	(2.6)	32.70	(0.15)	8.36	(0.4)	−2.6	(2.4)
	C	5.85	(0.20)	15.31	(2.70)	76.0	(5.4)	11.192	(0.20)	6.38	(1.4)	63.4	(6.6)
	S	34.93	(0.27)	5.41	(0.65)	51.7	(3.9)	67.30	(0.27)	2.22	(0.3)	36.9	(4.9)
0213+412	N	14.03	(0.12)	1.49	(0.73)	65.6	(12.8)	29.97	(0.12)	3.99	(0.4)	34.3	(3.3)
	C	99.21	(0.14)	3.71	(0.23)	84.2	(2.7)	136.64	(0.14)	2.80	(0.2)	77.2	(2.6)
	S	27.73	(0.15)	3.33	(0.47)	74.1	(4.4)	55.07	(0.15)	3.14	(0.3)	64.0	(3.1)
0222+422A	N	22.10	(0.16)	1.32	(0.61)	47.4	(12.2)	46.59	(0.16)	0.62	(0.3)	−68.2	(12.9)
	S	9.92	(0.19)	8.90	(1.54)	65.7	(5.3)	19.10	(0.19)	5.15	(0.8)	71.4	(4.8)
0228+409A	E	13.81	(0.15)	4.84	(0.87)	−53.7	(5.5)	24.12	(0.15)	4.16	(0.5)	−80.2	(4.0)
	W	40.80	(0.17)	4.93	(0.39)	5.1	(3.0)	76.04	(0.17)	3.40	(0.2)	−6.9	(2.8)
0254+406	N	21.03	(0.21)	5.51	(0.84)	20.5	(4.7)	43.43	(0.21)	5.31	(0.4)	25.2	(3.0)
	S	62.31	(0.19)	0.53	(0.32)	−8.4	(14.8)	106.41	(0.19)	0.85	(0.2)	−24.4	(7.1)
0255+460	E	39.93	(0.13)	0.00	(0.33)	−44.1	(49.8)	75.27	(0.13)	0.00	(0.2)	60.5	(39.7)
	W	93.24	(0.14)	0.85	(0.23)	−28.4	(7.8)	167.23	(0.14)	0.25	(0.2)	48.9	(15.6)
0701+392	E	20.68	(0.15)	6.99	(0.61)	3.3	(3.2)	32.51	(0.15)	3.64	(0.4)	40.1	(3.7)
	W	85.20	(0.17)	0.82	(0.26)	−72.2	(8.8)	144.33	(0.17)	0.17	(0.2)	27.3	(20.6)
0729+437	N	14.38	(0.14)	8.45	(0.83)	38.4	(3.4)	22.45	(0.14)	6.45	(0.5)	37.9	(3.1)
	S	67.47	(0.16)	2.37	(0.27)	−44.4	(3.8)	111.37	(0.16)	0.74	(0.2)	−46.2	(7.3)
0744+464	E	9.09	(0.14)	1.28	(1.23)	12.5	(20.1)	18.53	(0.14)	0.37	(0.6)	50.8	(25.1)
	C	2.56	(0.10)	5.64	(3.14)	53.3	(16.0)	2.93	(0.10)	3.00	(2.7)	69.6	(26.1)
	W	71.46	(0.15)	5.72	(0.26)	−82.4	(2.4)	124.87	(0.15)	1.87	(0.2)	51.3	(3.4)
†0754+396	N	12.57	(0.20)	24.02	(1.28)	82.7	(2.5)	28.83	(0.20)	24.73	(0.6)	85.1	(2.1)
	S	64.02	(0.19)	9.56	(0.31)	81.3	(2.2)	117.91	(0.19)	7.86	(0.2)	79.3	(2.1)
0805+406	E	54.26	(0.18)	9.75	(0.33)	−26.9	(2.2)	80.22	(0.18)	9.38	(0.2)	−23.4	(2.1)
	W	73.42	(0.21)	4.39	(0.31)	−15.4	(2.8)	97.08	(0.21)	4.42	(0.2)	−12.8	(2.5)
	NW	8.17	(0.19)	17.26	(1.90)	−43.5	(3.7)	14.65	(0.19)	5.32	(1.1)	−16.2	(5.9)
	SW	3.75	(0.16)	8.10	(3.48)	−15.5	(11.5)	6.64	(0.16)	4.86	(2.0)	48.0	(10.9)
†0809+404	E	263.37	(0.17)	3.70	(0.21)	54.5	(2.6)	407.64	(0.17)	1.31	(0.2)	49.2	(3.9)
	W	3.45	(0.14)	16.93	(3.18)	63.1	(5.6)	4.13	(0.14)	3.51	(2.7)	35.8	(17.2)
0810+460B	N	73.50	(0.14)	0.15	(0.25)	−21.1	(24.1)	140.27	(0.14)	0.00	(0.2)	−15.3	(119.8)
	S	83.25	(0.15)	2.70	(0.25)	−3.5	(3.3)	144.85	(0.15)	0.74	(0.2)	−0.7	(6.8)
0814+441	E	22.28	(0.20)	2.40	(0.74)	−1.4	(8.7)	40.02	(0.20)	0.84	(0.4)	13.2	(13.1)
	C	9.27	(0.13)	3.99	(1.10)	−23.5	(8.1)	12.41	(0.13)	1.21	(0.8)	56.6	(19.4)
	W	11.51	(0.35)	17.06	(2.47)	−70.6	(4.6)	22.70	(0.35)	3.78	(1.3)	82.8	(9.2)

Table A.2. continued.

		8.5 GHz						4.9 GHz					
Name	c	S_I (mJy)		m_v(%)		χ(°)		S_I (mJy)		m_v(%)		χ(°)	
0856+406	E	9.60	(0.12)	0.99	(1.06)	−65.3	(21.6)	24.56	(0.12)	0.34	(0.4)	54.8	(22.6)
	W	5.72	(0.12)	14.81	(1.76)	−52.2	(3.9)	13.75	(0.12)	1.60	(0.7)	−66.7	(12.2)
0930+389	N	20.90	(0.14)	3.33	(0.58)	48.9	(5.3)	36.60	(0.14)	2.30	(0.3)	−79.5	(4.7)
	S	21.24	(0.15)	2.98	(0.60)	53.4	(6.0)	37.35	(0.15)	2.20	(0.3)	−81.5	(5.0)
0935+428A	E	34.60	(0.13)	2.07	(0.36)	−52.8	(5.3)	63.30	(0.13)	0.00	(0.2)	10.9	(37.5)
	W	32.80	(0.13)	1.04	(0.38)	−16.8	(10.0)	57.90	(0.13)	0.00	(0.2)	13.2	(34.8)
0951+422	N	45.53	(0.17)	4.74	(0.36)	0.5	(2.9)	70.46	(0.17)	3.95	(0.2)	2.4	(2.7)
	C	46.84	(0.13)	8.06	(0.30)	−36.5	(2.3)	62.49	(0.13)	2.21	(0.2)	−42.4	(3.5)
	S	14.70	(0.12)	4.96	(0.68)	76.1	(4.3)	28.46	(0.12)	0.83	(0.4)	68.3	(11.8)
0955+390	E	37.98	(0.28)	11.48	(0.62)	16.3	(2.5)	63.83	(0.28)	10.24	(0.4)	13.5	(2.3)
	C	3.61	(0.15)	1.06	(3.33)	3.0	(89.9)	3.70	(0.15)	3.13	(3.2)	−66.9	(29.6)
	W	51.81	(0.27)	6.86	(0.46)	−23.1	(2.8)	85.27	(0.27)	5.85	(0.3)	−16.3	(2.5)
1025+390B	N	32.01	(0.15)	5.35	(0.42)	−34.1	(3.0)	50.53	(0.15)	2.86	(0.3)	−61.0	(3.4)
	C	140.66	(0.21)	1.65	(0.23)	−63.1	(4.5)	171.32	(0.21)	2.95	(0.2)	−87.9	(2.7)
	S	53.46	(0.19)	5.06	(0.35)	72.7	(2.8)	89.08	(0.19)	5.56	(0.2)	85.4	(2.3)
†1039+424	N	11.17	(0.19)	23.56	(1.36)	−79.0	(2.6)	26.40	(0.19)	24.70	(0.6)	−73.2	(2.1)
	S	22.80	(0.15)	2.33	(0.56)	−24.1	(7.0)	43.82	(0.15)	4.22	(0.3)	2.6	(2.9)
†1044+454	N	39.63	(0.14)	8.53	(0.35)	37.0	(2.3)	86.16	(0.14)	4.47	(0.2)	83.6	(2.4)
	S	1.27	(0.10)	32.53	(6.29)	−23.8	(5.8)	3.26	(0.10)	5.57	(2.5)	−50.1	(11.7)
†1055+404A	N	4.50	(0.10)	3.24	(1.79)	45.2	(14.1)	4.08	(0.10)	1.91	(2.0)	−33.2	(20.3)
	C	60.61	(0.15)	6.95	(0.28)	−1.8	(2.3)	102.95	(0.15)	6.20	(0.2)	−4.8	(2.2)
	S	7.67	(0.19)	14.46	(1.96)	−42.7	(4.3)	14.31	(0.19)	8.51	(1.1)	−51.7	(4.0)
†1136+420	W	107.15	(0.17)	2.10	(0.24)	56.1	(3.8)	167.40	(0.17)	0.22	(0.2)	−8.4	(17.6)
	E	2.12	(0.12)	20.67	(4.67)	−2.2	(6.6)	5.55	(0.12)	5.73	(1.8)	−13.9	(8.8)
1143+456	N	9.19	(0.11)	1.47	(0.94)	−64.1	(15.3)	20.75	(0.11)	0.00	(0.4)	−3.6	(46.6)
	S	55.68	(0.13)	1.41	(0.27)	74.8	(5.8)	116.74	(0.13)	0.08	(0.2)	21.7	(26.3)
1157+460	N	127.37	(0.13)	0.72	(0.22)	45.8	(8.5)	218.32	(0.13)	0.00	(0.2)	85.3	(115.5)
	S	59.25	(0.12)	1.12	(0.26)	27.3	(6.7)	118.11	(0.12)	0.20	(0.2)	35.1	(18.6)
	W	13.84	(0.10)	0.69	(0.64)	35.7	(19.1)	27.37	(0.10)	0.00	(0.3)	57.5	(127.0)
1201+394	N	32.92	(0.19)	5.11	(0.51)	57.8	(3.5)	54.21	(0.19)	3.91	(0.3)	47.1	(3.1)
	S	65.85	(0.18)	6.34	(0.30)	−21.0	(2.4)	104.89	(0.18)	6.63	(0.2)	−15.4	(2.2)
1204+401	N	22.98	(0.20)	9.28	(0.72)	−28.0	(3.0)	39.94	(0.20)	7.67	(0.4)	−27.3	(2.6)
	S	9.03	(0.14)	7.57	(1.29)	56.6	(5.2)	18.49	(0.14)	0.71	(0.6)	−61.2	(19.4)
1216+402	N	23.46	(0.21)	11.77	(0.73)	85.0	(2.7)	42.27	(0.21)	8.85	(0.4)	74.4	(2.4)
	S	37.62	(0.24)	1.40	(0.54)	12.1	(10.6)	63.62	(0.24)	3.61	(0.3)	1.1	(3.3)
1217+427	N	33.60	(0.13)	0.56	(0.37)	−58.1	(16.0)	57.70	(0.13)	0.00	(0.2)	50.5	(38.1)
	S	18.40	(0.13)	3.26	(0.60)	−40.1	(5.6)	31.50	(0.13)	0.83	(0.4)	−22.4	(11.8)
1220+408	N	13.69	(0.20)	2.18	(1.19)	−61.3	(13.8)	23.71	(0.20)	1.91	(0.7)	−18.4	(9.9)
	C1	3.01	(0.13)	4.61	(3.48)	31.8	(17.6)	4.25	(0.13)	0.00	(2.5)	−69.9	(35.0)
	C2	8.39	(0.10)	3.84	(0.97)	65.4	(7.3)	13.06	(0.10)	2.87	(0.6)	80.3	(6.4)
	S	39.45	(0.19)	11.49	(0.44)	52.2	(2.3)	72.99	(0.19)	9.56	(0.3)	56.5	(2.1)
1233+418	N	69.44	(0.16)	9.66	(0.27)	−10.4	(2.2)	103.29	(0.16)	7.03	(0.2)	−14.6	(2.2)
	S	114.70	(0.16)	0.76	(0.23)	−24.9	(8.5)	164.27	(0.16)	0.31	(0.2)	−15.0	(13.9)
1241+411	E	24.65	(0.14)	0.93	(0.51)	−14.9	(13.9)	37.70	(0.14)	0.00	(0.3)	−28.7	(51.4)
	W	82.10	(0.13)	0.66	(0.24)	−61.3	(9.8)	119.71	(0.13)	0.22	(0.2)	6.6	(17.8)
1350+432	N	7.82	(0.14)	7.54	(1.42)	70.7	(5.6)	18.21	(0.14)	1.97	(0.6)	82.2	(8.8)
	S	4.62	(0.12)	14.41	(2.04)	70.9	(4.5)	10.40	(0.12)	10.92	(0.9)	−81.9	(3.1)
1458+433	N	46.33	(0.14)	1.86	(0.32)	4.6	(5.2)	77.42	(0.14)	2.95	(0.2)	2.5	(2.9)
	C	20.52	(0.11)	3.80	(0.48)	40.9	(4.1)	32.16	(0.11)	4.71	(0.3)	42.5	(2.8)
	S	22.58	(0.16)	1.38	(0.59)	−0.6	(11.4)	37.39	(0.16)	2.45	(0.4)	13.4	(4.7)
2322+403	N	12.72	(0.15)	4.21	(0.98)	54.9	(6.8)	23.99	(0.15)	2.05	(0.5)	38.9	(7.4)
	S	36.19	(0.15)	6.31	(0.39)	38.8	(2.7)	72.05	(0.15)	2.51	(0.2)	7.7	(3.3)
2302+402	N	194.00	(0.13)	0.32	(0.21)	−7.9	(15.9)	375.50	(0.13)	0.00	(0.2)	35.7	(129.4)
	S	35.70	(0.11)	1.56	(0.32)	−61.9	(6.0)	71.90	(0.11)	0.32	(0.2)	71.8	(14.7)
2311+469	N	255.00	(0.14)	9.75	(0.21)	−71.3	(2.1)	422.50	(0.14)	8.85	(0.2)	−67.4	(2.1)
	C	46.17	(0.10)	1.35	(0.26)	26.7	(5.8)	58.74	(0.10)	1.14	(0.2)	5.1	(5.3)
	S	111.60	(0.12)	1.73	(0.22)	49.6	(4.1)	221.70	(0.12)	0.00	(0.2)	72.9	(136.8)
2349+410	N	17.20	(0.12)	0.78	(0.60)	−28.5	(17.9)	39.70	(0.12)	0.47	(0.3)	38.2	(15.3)
	S	47.40	(0.12)	0.67	(0.28)	−38.1	(11.5)	85.80	(0.12)	0.00	(0.2)	2.4	(38.1)

Table A.3. *Low Resolution* data (error in parenthesis).

	8.5 GHz						4.9 GHz						1.4 GHz					
Name	$S_{\rm I}$ (mJy)		m_v(%)		$\chi(^\circ)$		$S_{\rm I}$ (mJy)		m_v(%)		$\chi(^\circ)$		$S_{\rm I}$ (mJy)		m_v(%)		$\chi(^\circ)$	
0003+387	45.53	(0.20)	2.10	(0.41)	31.9	(5.8)	105.36	(0.20)	0.80	(0.2)	1.9	(7.7)	482.4	(14.5)	−0.06	(0.08)	0.0	(0.0)
†0034+444	92.16	(0.20)	3.05	(0.26)	26.2	(3.2)	183.49	(0.20)	2.98	(0.2)	36.8	(2.6)	674.9	(20.3)	0.36	(0.06)	−1.3	(3.4)
0039+373	117.40	(0.10)	0.74	(0.21)	−41.7	(8.1)	252.70	(0.10)	0.35	(0.2)	80.5	(11.8)	938.8	(28.2)	0.17	(0.05)	−77.3	(5.4)
0039+391	34.90	(0.13)	0.96	(0.36)	−28.1	(10.1)	74.60	(0.13)	0.00	(0.2)	−5.6	(42.8)	315.0	(9.5)	0.19	(0.13)	−77.5	(13.7)
0039+398	118.53	(0.22)	0.26	(0.25)	89.5	(19.8)	226.74	(0.22)	0.00	(0.2)	−62.9	(37.2)	748.3	(22.5)	0.33	(0.06)	76.3	(3.4)
0039+412	76.30	(0.25)	5.19	(0.33)	−79.5	(2.7)	131.05	(0.25)	5.18	(0.2)	82.8	(2.3)	371.4	(11.2)	1.79	(0.12)	26.7	(1.3)
0041+425	71.80	(0.10)	2.19	(0.23)	72.4	(3.6)	137.50	(0.10)	0.43	(0.2)	35.7	(10.2)	463.2	(13.9)	0.17	(0.09)	23.6	(10.5)
0049+379	76.39	(0.22)	7.06	(0.31)	−17.1	(2.4)	174.83	(0.22)	1.68	(0.2)	9.2	(3.7)	792.9	(23.8)	0.06	(0.06)	−26.7	(19.0)
†0110+401	177.85	(0.24)	5.33	(0.23)	86.4	(2.3)	256.30	(0.24)	4.94	(0.2)	83.1	(2.2)	546.3	(16.4)	4.20	(0.08)	−66.8	(0.4)
0120+405	87.77	(0.22)	5.24	(0.28)	51.2	(2.5)	169.27	(0.22)	3.78	(0.2)	1.0	(2.4)	608.5	(18.3)	0.24	(0.07)	−15.4	(5.6)
†0123+402	38.11	(0.18)	4.65	(0.43)	78.9	(3.3)	74.73	(0.18)	4.03	(0.2)	58.4	(2.6)	256.3	(7.7)	−0.06	(0.16)	0.0	(0.0)
0128+394	41.61	(0.23)	0.60	(0.48)	−38.2	(17.8)	85.23	(0.23)	1.55	(0.3)	−86.1	(5.1)	326.6	(9.8)	1.09	(0.12)	83.8	(2.2)
0137+401	55.68	(0.27)	1.64	(0.43)	84.6	(7.5)	95.04	(0.27)	1.67	(0.3)	44.1	(5.0)	287.5	(10.2)	1.01	(0.15)	17.3	(2.8)
0140+387	29.68	(0.19)	2.05	(0.54)	−25.2	(7.5)	77.13	(0.19)	0.27	(0.2)	27.4	(19.0)	425.9	(12.8)	0.00	(0.09)	0.0	(0.0)
0144+432	60.63	(0.37)	3.53	(0.52)	31.2	(4.6)	111.18	(0.37)	2.90	(0.3)	16.5	(3.6)	334.2	(10.0)	1.38	(0.12)	64.0	(1.6)
0147+400	189.00	(0.10)	0.00	(0.20)	88.3	(55.1)	281.10	(0.10)	0.00	(0.2)	43.0	(407.6)	716.3	(21.5)	0.26	(0.05)	15.4	(4.2)
0213+412	140.97	(0.23)	3.37	(0.24)	81.4	(2.8)	221.68	(0.23)	2.61	(0.2)	67.3	(2.7)	541.5	(16.3)	0.34	(0.08)	88.8	(4.6)
0222+422A	32.02	(0.25)	3.58	(0.65)	61.0	(5.5)	65.69	(0.25)	1.64	(0.3)	79.9	(6.1)	259.6	(7.8)	0.38	(0.16)	75.6	(8.3)
0228+409A	55.52	(0.26)	3.50	(0.43)	−9.3	(4.0)	101.56	(0.26)	1.77	(0.2)	−16.2	(4.5)	350.8	(10.5)	1.16	(0.13)	−46.4	(2.1)
0254+406	84.10	(0.32)	1.83	(0.36)	13.1	(5.9)	151.04	(0.32)	1.66	(0.2)	13.5	(4.3)	497.0	(14.9)	1.34	(0.09)	−47.8	(1.3)
0255+460	133.18	(0.19)	0.63	(0.23)	−29.7	(10.1)	242.50	(0.19)	0.19	(0.2)	50.9	(18.6)	713.6	(21.4)	0.15	(0.07)	80.7	(8.9)
0701+392	107.54	(0.25)	0.82	(0.27)	−12.9	(9.3)	179.75	(0.25)	0.89	(0.2)	37.0	(6.2)	503.3	(15.1)	0.22	(0.09)	−74.6	(7.6)
0703+468	393.70	(0.10)	0.16	(0.20)	−42.0	(22.6)	621.60	(0.10)	0.00	(0.2)	−89.1	(53.5)	1584.9	(47.5)	0.00	(0.03)	0.0	(0.0)
0722+393A	125.76	(0.18)	0.45	(0.23)	−8.0	(13.1)	254.40	(0.18)	0.00	(0.2)	50.2	(55.4)	1104.7	(33.1)	0.12	(0.04)	−86.5	(6.1)
0729+437	81.85	(0.21)	0.55	(0.29)	−27.2	(13.3)	133.82	(0.21)	0.44	(0.2)	30.5	(11.8)	385.5	(11.6)	0.17	(0.11)	67.6	(12.4)
0744+464	83.10	(0.22)	4.74	(0.29)	−83.7	(2.7)	146.33	(0.22)	1.74	(0.2)	51.9	(3.7)	513.7	(15.4)	0.31	(0.08)	−70.4	(4.9)
†0748+413	22.35	(0.19)	15.62	(0.72)	−32.7	(2.4)	43.36	(0.19)	7.31	(0.4)	−37.9	(2.5)	234.5	(7.0)	0.65	(0.18)	31.9	(5.4)
†0754+396	76.59	(0.27)	11.93	(0.35)	81.8	(2.2)	146.74	(0.27)	11.12	(0.2)	81.8	(2.1)	544.8	(16.3)	7.96	(0.08)	−88.7	(0.2)
†0800+472	213.25	(0.20)	2.25	(0.21)	−42.3	(3.4)	322.98	(0.20)	1.49	(0.2)	−52.2	(3.6)	888.2	(26.6)	0.44	(0.05)	88.4	(2.1)
0805+406	139.61	(0.37)	6.99	(0.29)	−25.1	(2.3)	198.59	(0.37)	6.13	(0.2)	−18.8	(2.2)	530.1	(15.9)	4.63	(0.08)	35.8	(0.3)
†0809+404	266.82	(0.22)	3.87	(0.21)	54.9	(2.5)	411.77	(0.22)	1.34	(0.2)	48.8	(3.9)	1062.1	(31.9)	0.12	(0.04)	87.5	(6.3)
0810+460B	156.75	(0.21)	1.53	(0.23)	−4.9	(4.6)	285.12	(0.21)	0.37	(0.2)	−1.4	(11.6)	1106.1	(33.2)	0.13	(0.04)	61.0	(5.6)
0814+441	43.07	(0.43)	3.87	(0.81)	−57.7	(6.2)	75.13	(0.43)	0.94	(0.5)	69.5	(13.0)	289.2	(8.7)	1.01	(0.13)	−37.2	(2.6)
0822+394	180.90	(0.10)	0.00	(0.20)	10.2	(123.9)	335.10	(0.10)	0.00	(0.2)	−76.5	(65.0)	1198.3	(42.3)	0.08	(0.04)	−77.0	(8.8)
0840+424A	371.90	(0.10)	0.00	(0.20)	−47.7	(42.6)	568.40	(0.10)	0.00	(0.2)	−84.1	(48.0)	1409.7	(42.3)	0.12	(0.03)	9.6	(4.6)
0856+406	15.32	(0.18)	6.30	(0.94)	−53.9	(4.7)	38.31	(0.18)	0.42	(0.4)	−83.4	(19.9)	240.0	(7.2)	0.00	(0.00)	0.0	(0.0)
0902+416	130.87	(0.18)	1.29	(0.23)	−3.0	(5.4)	199.99	(0.18)	0.23	(0.2)	−82.2	(17.0)	496.1	(14.9)	0.14	(0.09)	49.5	(12.1)
0930+389	42.85	(0.22)	2.88	(0.46)	50.7	(4.9)	74.53	(0.22)	2.25	(0.3)	−79.3	(4.1)	283.6	(8.5)	0.71	(0.15)	13.7	(4.1)
0935+428A	67.40	(0.19)	1.31	(0.30)	−41.7	(6.6)	121.20	(0.19)	0.00	(0.2)	12.1	(30.6)	438.6	(13.2)	0.13	(0.09)	−83.3	(13.7)
0951+422	107.07	(0.24)	3.86	(0.27)	−25.6	(2.8)	161.41	(0.24)	1.77	(0.2)	−9.8	(3.7)	428.1	(12.8)	0.66	(0.10)	−3.3	(2.8)
0955+390	93.39	(0.42)	6.60	(0.41)	−1.0	(2.7)	152.81	(0.42)	6.50	(0.3)	0.5	(2.3)	459.8	(13.8)	4.48	(0.10)	39.4	(0.4)
1007+422	89.10	(0.10)	3.94	(0.22)	−7.4	(2.6)	146.30	(0.10)	0.40	(0.2)	−80.5	(10.7)	429.7	(12.9)	0.17	(0.10)	−47.5	(11.3)
1008+423	148.30	(0.10)	0.05	(0.21)	−54.0	(27.8)	233.40	(0.10)	0.00	(0.2)	−35.7	(32.5)	592.8	(17.8)	−0.01	(0.07)	0.0	(0.0)
1016+443	38.80	(0.10)	0.50	(0.29)	13.2	(14.4)	79.90	(0.10)	0.00	(0.2)	−74.9	(51.1)	353.9	(10.6)	0.08	(0.11)	−71.9	(26.8)
1025+390B	226.14	(0.32)	1.56	(0.23)	−73.3	(4.6)	310.93	(0.32)	3.46	(0.2)	−87.6	(2.5)	658.1	(19.7)	0.00	(0.00)	0.0	(0.0)
†1027+392	105.00	(0.25)	0.28	(0.28)	82.7	(20.2)	158.70	(0.25)	1.19	(0.2)	−85.2	(5.0)	384.8	(11.6)	1.04	(0.11)	89.1	(2.1)
†1039+424	33.97	(0.24)	7.34	(0.60)	−73.1	(3.1)	70.02	(0.24)	7.07	(0.3)	−68.1	(2.4)	277.0	(8.3)	4.24	(0.14)	−38.9	(0.7)
†1044+454	40.90	(0.17)	7.77	(0.39)	33.8	(2.5)	89.42	(0.17)	4.30	(0.2)	85.1	(2.4)	440.2	(13.2)	−0.05	(0.09)	0.0	(0.0)
1049+384	104.30	(0.10)	0.00	(0.21)	−88.3	(31.9)	198.60	(0.10)	0.00	(0.2)	85.5	(43.6)	682.4	(20.5)	0.04	(0.06)	−89.7	(31.8)
†1055+404A	72.78	(0.26)	6.12	(0.35)	−7.9	(2.6)	117.34	(0.26)	5.61	(0.2)	−10.6	(2.3)	368.7	(11.1)	4.13	(0.12)	13.0	(0.5)
1128+455	395.85	(0.21)	0.17	(0.20)	−81.1	(21.9)	671.47	(0.21)	0.08	(0.2)	58.7	(25.0)	2048.8	(80.7)	0.06	(0.02)	66.7	(6.4)
1133+432	282.10	(0.10)	0.00	(0.20)	18.4	(32.6)	493.20	(0.10)	0.00	(0.2)	31.6	(95.1)	1448.8	(43.5)	0.06	(0.03)	−42.3	(9.1)
†1136+383	115.80	(0.10)	0.14	(0.21)	−1.0	(23.4)	175.60	(0.10)	0.00	(0.2)	9.6	(37.2)	460.0	(13.8)	0.03	(0.10)	−54.9	(65.5)
1136+420	109.27	(0.21)	1.89	(0.25)	50.6	(4.3)	172.95	(0.21)	0.42	(0.2)	−10.7	(11.3)	458.7	(13.8)	0.26	(0.10)	−41.9	(7.2)
1143+456	64.87	(0.17)	1.27	(0.29)	80.3	(6.7)	137.49	(0.17)	0.05	(0.2)	17.0	(27.1)	710.7	(21.3)	−0.01	(0.05)	0.0	(0.0)
1157+460	200.46	(0.20)	0.81	(0.22)	38.0	(7.6)	363.80	(0.20)	0.00	(0.2)	43.9	(50.1)	1156.5	(34.7)	0.01	(0.03)	−29.4	(44.9)
1159+395	162.90	(0.10)	0.00	(0.21)	−37.4	(30.9)	249.20	(0.10)	0.00	(0.2)	67.3	(128.7)	605.8	(18.2)	0.07	(0.08)	54.7	(20.0)

Table A.3. continued.

	8.5 GHz						4.9 GHz						1.4 GHz					
Name	S_I (mJy)		m_v(%)		χ(°)		S_I (mJy)		m_v(%)		χ(°)		S_I (mJy)		m_v(%)		χ(°)	
1201+394	103.23	(0.29)	2.57	(0.30)	−14.8	(3.9)	167.35	(0.29)	3.41	(0.2)	−6.9	(2.6)	482.6	(14.5)	0.53	(0.09)	70.7	(3.3)
1204+401	32.01	(0.25)	4.36	(0.65)	−26.8	(4.6)	58.42	(0.25)	5.36	(0.4)	−28.8	(2.8)	259.0	(7.8)	0.07	(0.17)	−51.0	(50.5)
1212+380	33.73	(0.18)	0.35	(0.47)	37.8	(23.2)	63.65	(0.18)	0.52	(0.3)	34.1	(13.7)	293.4	(8.8)	0.13	(0.15)	−74.6	(21.3)
1216+402	61.09	(0.32)	3.77	(0.46)	81.1	(4.0)	105.89	(0.32)	2.06	(0.3)	57.1	(4.3)	365.9	(11.0)	0.82	(0.12)	−40.7	(2.8)
1217+427	52.00	(0.19)	1.50	(0.35)	−44.9	(6.8)	89.20	(0.19)	0.07	(0.2)	−14.5	(27.7)	302.8	(9.1)	0.17	(0.13)	−12.0	(15.2)
1220+408	64.55	(0.31)	7.34	(0.43)	53.9	(2.6)	114.01	(0.31)	5.95	(0.3)	57.0	(2.4)	463.5	(13.9)	0.27	(0.09)	−61.3	(6.7)
1225+442	63.40	(0.10)	0.00	(0.24)	−31.6	(38.3)	110.10	(0.10)	0.00	(0.2)	−22.4	(37.1)	383.8	(11.5)	0.42	(0.10)	−45.2	(4.8)
1233+418	185.24	(0.23)	4.05	(0.22)	−12.1	(2.5)	269.01	(0.23)	2.91	(0.2)	−14.6	(2.6)	690.5	(20.7)	0.15	(0.07)	−37.5	(8.1)
1241+411	106.74	(0.19)	0.53	(0.25)	−49.0	(12.3)	157.41	(0.19)	0.14	(0.2)	1.3	(22.2)	361.0	(10.8)	−0.03	(0.12)	0.0	(0.0)
1242+410	465.00	(0.10)	0.47	(0.20)	−13.8	(11.4)	655.70	(0.10)	0.00	(0.2)	9.2	(44.6)	1341.8	(40.3)	0.06	(0.03)	−62.7	(10.8)
1314+453A	144.20	(0.10)	0.28	(0.21)	18.4	(17.2)	228.50	(0.10)	0.00	(0.2)	−89.4	(100.5)	667.3	(20.0)	0.10	(0.06)	−72.0	(11.0)
1340+439	66.20	(0.10)	0.60	(0.23)	67.3	(10.6)	129.60	(0.10)	0.00	(0.2)	44.6	(60.1)	546.7	(16.4)	0.68	(0.07)	−34.1	(2.1)
†1343+386	276.70	(0.10)	2.38	(0.20)	89.6	(3.1)	378.80	(0.10)	2.83	(0.2)	−75.9	(2.5)	895.3	(26.9)	0.45	(0.05)	85.6	(2.1)
1350+432	12.54	(0.20)	9.69	(1.29)	68.0	(4.3)	29.42	(0.20)	5.60	(0.6)	−83.9	(3.5)	169.7	(5.1)	3.39	(0.23)	−80.1	(1.3)
1432+428B	245.00	(0.10)	0.00	(0.20)	80.5	(44.9)	381.50	(0.10)	0.00	(0.2)	34.0	(306.4)	912.1	(32.2)	0.20	(0.05)	−26.8	(4.4)
1458+433	89.43	(0.24)	1.76	(0.29)	17.3	(5.1)	146.97	(0.24)	2.63	(0.2)	16.7	(2.9)	438.4	(13.2)	2.36	(0.09)	4.6	(0.7)
1441+409	208.40	(0.10)	1.08	(0.20)	−1.2	(5.6)	343.10	(0.10)	0.00	(0.2)	62.3	(121.9)	963.4	(28.9)	0.08	(0.05)	−61.1	(11.4)
1449+421	64.50	(0.10)	0.00	(0.24)	72.3	(35.6)	145.70	(0.10)	0.00	(0.2)	−76.5	(29.8)	813.5	(24.4)	0.13	(0.06)	−26.9	(7.9)
2301+443	114.48	(0.18)	0.50	(0.24)	55.6	(12.5)	260.32	(0.18)	0.24	(0.2)	28.6	(16.0)	1229.4	(36.9)	0.18	(0.04)	−33.0	(4.0)
2302+402	229.62	(0.10)	0.27	(0.20)	−30.1	(17.4)	447.36	(0.10)	0.00	(0.2)	61.2	(58.0)	1162.9	(34.9)	0.67	(0.04)	51.3	(1.1)
2304+377	314.80	(0.10)	2.90	(0.20)	10.9	(2.8)	560.50	(0.10)	1.19	(0.2)	23.9	(4.1)	1487.1	(44.6)	0.12	(0.03)	75.7	(4.5)
2311+469	412.76	(0.10)	5.68	(0.20)	−73.6	(2.2)	702.88	(0.10)	5.24	(0.2)	−67.1	(2.2)	1927.5	(57.8)	3.52	(0.02)	−86.1	(0.1)
2322+403	49.25	(0.24)	5.67	(0.44)	39.6	(3.0)	97.14	(0.24)	2.30	(0.2)	17.2	(3.7)	318.3	(9.6)	−0.02	(0.13)	0.0	(0.0)
2330+402	183.90	(0.10)	0.00	(0.20)	76.5	(48.1)	323.80	(0.10)	0.00	(0.2)	−11.6	(184.6)	831.5	(24.9)	0.25	(0.05)	76.5	(4.0)
2348+450	116.70	(0.10)	1.99	(0.21)	39.9	(3.6)	227.60	(0.10)	0.51	(0.2)	57.0	(8.5)	741.9	(22.3)	0.07	(0.06)	−18.9	(16.9)
2349+410	64.61	(0.10)	0.73	(0.24)	−34.9	(8.9)	125.47	(0.10)	0.15	(0.2)	26.1	(21.1)	452.5	(13.6)	0.49	(0.09)	−62.8	(3.5)
2358+406	359.00	(0.10)	0.46	(0.20)	44.1	(11.6)	573.30	(0.10)	0.00	(0.2)	41.7	(272.4)	1300.2	(39.0)	0.07	(0.03)	−35.6	(8.3)